



Original Paper

Synthesis and transport characteristics of multi-color fluorescent silica nanoparticle tracer in sandstone cores



Fang-Jun Jia ^a, Hai-Tao Li ^{a,*}, Zi-Min Liu ^{b,**}, Xin Ma ^a, Guo-Qiang Zhang ^a, Qi-Hui Zhang ^a, Jie Li ^a

^a State Key Laboratory of Oil and Gas Reservoir Geology and Exploitation, Southwest Petroleum University, Chengdu, 610500, Sichuan, China

^b Chuanqing Drilling Engineering Co., Ltd., CNPC, Chengdu, 610051, Sichuan, China

ARTICLE INFO

Article history:

Received 16 October 2023

Received in revised form

4 December 2024

Accepted 29 December 2024

Available online 31 December 2024

Edited by Min Li

Keywords:

Chemical tracers

Fluorescence resonance energy transfer

Nanoparticles

Breakthrough curve

Particle transport

Sandstone reservoir

ABSTRACT

As an efficient monitoring and prediction tool, chemical tracers have been widely applied in reservoir characterization, production monitoring, water resources monitoring, and various other fields. Chemical tracer technology is characterized by high efficiency, high precision, relatively simple operational procedures, and low cost. Owing to the limitations of existing tracers, such as minimal options, limited transport efficiency, and complex detection methods, this study used fluorescein isothiocyanate and a ruthenium complex ($\text{Ru}(\text{phen}_3)^{2+}$) to synthesize 50 nm multi-color fluorescent silica nanoparticle tracers using an improved Stöber method based on fluorescence resonance energy transfer (FRET). Due to the FRET between the two compounds, the synthesized tracer exhibited the characteristics of multi-color fluorescence, and its fluorescent color varied with the mixing ratio of the two precursor solutions. The fluorescence intensity of the synthesized tracer was significantly higher than that of the monochromatic fluorescent nano-tracer. Fourier-transform infrared spectroscopy, ultraviolet spectrophotometry, and fluorescence spectrometry were used to characterize the structure, maximum absorption wavelength, and fluorescence characteristics of the synthesized tracer, respectively. The experimental results show that the synthesized tracer has a maximum absorption wavelength of 450 nm and an emission wavelength of 576 nm. Under field emission scanning electron microscopy, the tracer appears as uniformly spherical particles with a size of 50 ± 5 nm. It exhibited good dispersibility and fluorescence characteristics in reservoir environments that varied in temperature (25–85 °C) and salinity (1000–10000 mg/L). The effects of environmentally sensitive clay minerals, tracer particle size, injection concentration, fluid salinity, and flow rate on the transport characteristics (retention) of tracers in sandstone cores were studied using 12 sets of tracer breakthrough experiments. The experimental results showed that increased sensitivity to clay minerals, salinity, and tracer particle size were not conducive to tracer migration in the core. In contrast, increased tracer injection concentration and flow rate were beneficial to tracer migration in the core.

© 2025 The Authors. Publishing services by Elsevier B.V. on behalf of KeAi Communications Co. Ltd. This is an open access article under the CC BY-NC-ND license (<http://creativecommons.org/licenses/by-nc-nd/4.0/>).

1. Introduction

In oil and gas field expansion, waterflood development and tertiary oil recovery have become critical technical methods for increasing crude oil production (Li et al., 2021; Wang et al., 2019; Wang, 2021; Yi et al., 2021). Typically, information on the target

reservoir, such as reservoir heterogeneity, well connectivity, and inflow profile of the show well, directly affects water injection (or other injection fluids) and tertiary oil recovery (Ahmadi et al., 2011; Al-Shalabi et al., 2017; Sharma et al., 2014; Tan et al., 2019; Zhao et al., 2016). However, obtaining information on these underground reservoirs is challenging, and the simulation results of the most widely used numerical simulation methods significantly vary from the actual situation (Frooqnia, 2011). As the most conventional method, the production logging tool can only obtain reservoir information of the production or injection well based on its placement (App, 2017; Dhir and Datta, 2016; Davarpanah et al.,

* Corresponding author.

** Corresponding author.

E-mail addresses: haitao_li@163.com (H.-T. Li), dmlwasas@163.com (Z.-M. Liu).

2018; Jongkittinarukorn and Kitcharoen, 2010). Distributed optical fiber temperature measurements can effectively monitor the reservoir information of conventional and fractured horizontal wells (Luo et al., 2020, 2021). Other methods, including 3D seismic and micro-seismic logging technologies, have complex operations, low construction efficiency, and high cost (Alfataige et al., 2019; Bucior, 2013; Becker et al., 2015; Boersma et al., 2020; Mari et al., 2021; Wang et al., 2023). Chemical tracers are excellent reservoir monitoring tools widely used in oil and gas field development (Al-Qasim et al., 2020; Khaledialidusti and Kleppe, 2017; Li et al., 2021; Pedersen et al., 2021; Serres-Piole et al., 2012; Sanni et al., 2018; Silva et al., 2019; Tayyib et al., 2019). However, the stability of tracers in harsh reservoir environments varies depending on the type of tracer used. Ionic tracers, for instance, are generally stable under such conditions, while other tracers may exhibit instability. High temperature and salt contents, a weak acid/alkaline environment, numerous microbial activities, and complex fluids result in the decomposition of tracers, thus affecting the accuracy of the test results (Al-Shalabi et al., 2017; Bucior, 2013; Doorwar et al., 2020; Khaledialidusti and Kleppe, 2017; Li et al., 2021; Sanni et al., 2018; Silva et al., 2018; Velasco-Lozano and Balhoff, 2023). Therefore, the performance of the tracer itself is a crucial factor in determining its ability to track fluid movement and the reliability of the test results.

Nanoparticles are capable of consistently migrating through reservoir environments, exhibiting extended travel distances, and adapting to the challenging conditions typically found in reservoirs. These characteristics are necessary for oilfield tracers; therefore, scholars have recently conducted a series of studies on nanoparticles as oilfield tracer materials (Alaskar and Kosynkin, 2017; Alqahtani et al., 2018; Clemente et al., 2016; Ko and Huh, 2019; Khan et al., 2022; Pazini et al., 2023). The most common nanoparticle tracer is the fluorescent nanoparticle tracer, in which fluorescent dyes are incorporated into the nanoparticles during synthesis, imparting fluorescent properties to the particles. This technology has been widely used in bioimaging, but has rarely been reported for oil field tracers (Alaskar and Kosynkin, 2017). Hwang developed a carbon nanofluorescent tracer to detect the residual oil distribution in reservoirs (Hwang et al., 2012). Yang grafted three dyes, Rhodamine B, allyl oxy fluorescein, and acryloyl coumarin, onto polyacrylamide microspheres via suspension emulsion polymerization to determine the fluorescence ability of the synthesized polymer particles (Yang et al., 2020). However, the particles were approximately 200 μm in size, which could not meet the breakthrough in nanometer-sized pores. Murugesan synthesized 50 nm upconversion fluorescent nanoparticle tracers using YB-doped NaYF_4 as a sensitizer and Er and Tm as activators; however, the migration characteristics of the synthetic fluorescent nanoparticle tracers in the reservoir were unknown (Murugesan et al., 2020). Hu synthesized a carbon quantum dot nanofluorescent tracer with breakthrough ability and a minimum particle size of approximately 5 nm. However, only its migration characteristics in glass-filling columns were analyzed, and its characteristics in natural sandstone were not considered (Hu et al., 2019). Xu demonstrated the ability of multifunctional fluorescent nanoparticles to monitor multiple targets simultaneously but noted challenges like degradation and fluorescence signal attenuation under extreme conditions (Xu et al., 2022). Similarly, Zhao highlighted the advantages of fluorescent silica nanoparticles in monitoring dye migration in porous media, though stability, scalability, and environmental impacts remain concerns (Zhang et al., 2024). Chen showcased their potential in characterizing fluid dynamics in deep reservoirs but emphasized the need for improved stability, scalability, and ecological safety (Chen et al., 2023). Zhou summarized their benefits in enhancing oil recovery (EOR), particularly in fluid tracing

and reservoir characterization (Zhang et al., 2022). Together, these studies highlight the need to optimize nanoparticle design, especially for extreme environments and environmental safety, to advance practical applications. Compared with polymer nanoparticles, silica nanoparticles have more advantages, such as their size, which is generally between 1 and 100 nm. In contrast, silica nanoparticles have a high hydroxyl content, mechanical strength, and chemical stability, are non-toxic and pollution-free, and after surface modification, are better suited to harsh underground reservoir environments (Vitorge et al., 2013, 2014). Doping a fluorescent dye on the surface of nano-silica can overcome the dye decomposition of the fluorescence tracer, owing to the reservoir environment (Pareek et al., 2020). However, the quantum yield of inorganic dyes is relatively low, and single-luminescent doped nanoparticles lack rich color combinations, thus limiting their functionality (Stanzel et al., 2019). To produce multicolor tracers, a new strategy combines multiple energy-transfer fluorescent dyes with silica nanoparticles and adjusts the fluorescence resonance energy transfer (FRET)-mediated emission characteristics by changing the doping ratio of several tandem dyes (Kosynkin and Alaskar, 2016).

Fluorescein isothiocyanate (FITC) and $\text{Ru}(\text{phen}_3)^{2+}$ exhibit better fluorescence stability and obvious color development than other dyes. Simultaneously, the excitation and emission wavelengths of FITC and $\text{Ru}(\text{phen}_3)^{2+}$ overlap, respectively. The maximum wavelength is approximately 510 nm, and the gap is between 1.0 and 10 nm. FRET occurs between the two, and the mixture increases the fluorescence intensity. Therefore, we selected FITC and a ruthenium complex as fluorescent agents and synthesized multicolor fluorescent silica nano-tracers using FRET and sol-gel methods (He et al., 2021; Khurana et al., 2020; Liu et al., 2018; Sun et al., 2019). The tracer exhibited multiple colors, high fluorescence intensity, and controllable-scale characteristics. The fluorescence characteristics of the two fluorescent agents in different proportions were studied, and the dispersion and fluorescence stabilities of the fluorescent silica nano-tracers in reservoir environments (Temperature: 25–85 $^\circ\text{C}$, salinity: 1000–10000 mg/L) were investigated. The migration and retention characteristics of fluorescent silica nano-tracers in real sandstone cores were determined under different concentrations, particle sizes, injected water salinities, ambient temperatures, and rock characteristics. Their migration ability in natural sandstone reservoirs has been evaluated using experimental studies, which also confirm that this tracer can provide information about the reservoir.

2. Materials and methods

2.1. Reagents and materials

Tetraethyl orthosilicate (TEOS, purity > 99%), (3-aminopropyl) triethoxysilane (APTES, purity > 99%), ethanol (purity > 99%), FITC (purity > 99%), dichlorotris(1,10-phenanthroline) ruthenium(II) hydrate ($\text{Ru}(\text{phen}_3)^{2+}$, purity > 99%), ammonia water ($\text{NH}_3 \cdot \text{H}_2\text{O}$, purity > 28%), and deionized water (H_2O) were used in this experiment. All reagents were purchased from Aladdin Reagent and used as received without further purification. Pure water used in the experiments was prepared in-house.

2.2. Synthesis of the FRET@SiO₂ nanoparticle tracers

In this study, an improved sol technology was used to prepare fluorescent silica nanoparticles. Using the Stöber method (Li et al., 2023; Wang et al., 2021), we used the silane coupling agent APTES to functionalize the fluorescent dyes. First, precursor solutions of APTES-FITC and APTES- $\text{Ru}(\text{phen}_3)^{2+}$ were synthesized, and

the FITC isomer and $\text{Ru}(\text{phen}_3)_2^{2+}$ were grafted onto the silica nanoparticles such that the surfaces of the synthesized nano-silica were diverse and labelable. Simultaneously, the fluorescence properties and various synthetic tracers were enhanced via FRET between the two fluorescent dyes. The synthesis process is shown in Fig. 1. In 10 mL ethanol, 5 mg FITC and 9.2 mg $\text{Ru}(\text{phen}_3)_2^{2+}$ were dissolved and labeled as A and B solutions, respectively. To obtain the precursor solutions of the two fluorescent monomers, 28.43 mg of APTES was added to the aforementioned solution, and the mixture was stirred in the dark at 50 °C and 1000 rpm for 24 h. The two precursor solutions were then mixed in a 1:1 ratio to obtain solution C, which was added to 100 mL of ethanol solution containing 4 mL of ammonia. The mixture was stirred for 8 h to pre-hydrolyze the APTES-dye precursor solution. The mixed solution was added to TEOS (2.5 mL) and rested for 24 h to obtain the FRET@SiO₂ nanoparticle tracer. The temperature in the experiment was 40 °C, and the rotational speed was 1000 rpm. To collect the FRET@SiO₂ nanoparticle tracers, reactants were centrifuged for 10 min at 12000 rpm, and the centrifuged products were washed thrice with ethanol and deionized water to remove unreacted chemicals. The experimental products were dried in an incubator in the dark for characterization and other experiments. The molar volume ratio of FITC-to- $\text{Ru}(\text{phen}_3)_2^{2+}$ in the FRET@SiO₂ nanoparticle tracer used in subsequent experiments was 1:1.

2.3. Characterization of the FRET@SiO₂ nanoparticle tracer

The molecular structure of the FRET@SiO₂ nanoparticle tracer was characterized using infrared spectroscopy (Nicolet 6700, Thermo Scientific). The excitation wavelength of the fluorescent silica nanoparticles was measured using a UV spectrophotometer

(UV-2600, Shimadzu), with the maximum absorption wavelength considered as the excitation wavelength of the material, and their particle size was measured using a laser particle size analyzer (Master sizer 2000), with anhydrous ethanol as the solvent and at a temperature of 25 °C. The emission spectrum of the FRET@SiO₂ nanoparticle tracer at the maximum excitation wavelength was measured using a fluorescence spectrometer (Hitachi F-7000 DC-0506) for its quantitative detection. The micromorphology of the FRET@SiO₂ nanoparticle tracer was measured using field emission scanning electron microscopy under vacuum (FEI Quanta 650 FEG).

2.4. Adaptability of the FRET@SiO₂ nano-tracer in a reservoir environment

According to previous studies, the temperature and fluid salinity in a reservoir environment affect nanoparticle colloidal dispersion and fluorescence intensity, which affect particle migration and detection accuracy in porous media (Jiang et al., 2020; Lu et al., 2022; Xie et al., 2020). Therefore, it is necessary to explore the adaptability of FRET@SiO₂ nanoparticle tracers in reservoir environments. A 5 mg FRET@SiO₂ nanoparticle tracer was added to NaCl solutions of 1000, 5000, and 10000 ppm. In the first stage, the dispersion solution was ultrasonically dispersed for 40 min to completely scatter the particles. The dispersed solution rested at room temperature for 72 h, with 2 mL samples taken every 12 h to assess its zeta potential and fluorescence intensity, and the link between the experimental parameters and time was determined. The dispersion and fluorescence stabilities of the FRET@SiO₂ nanoparticle tracer was measured and evaluated over time using a zeta potentiometer and fluorescence spectrometer, respectively, at various salinities. For the temperature adaptation experiment, a 50 mg/L particle tracer distributed in deionized water was placed at

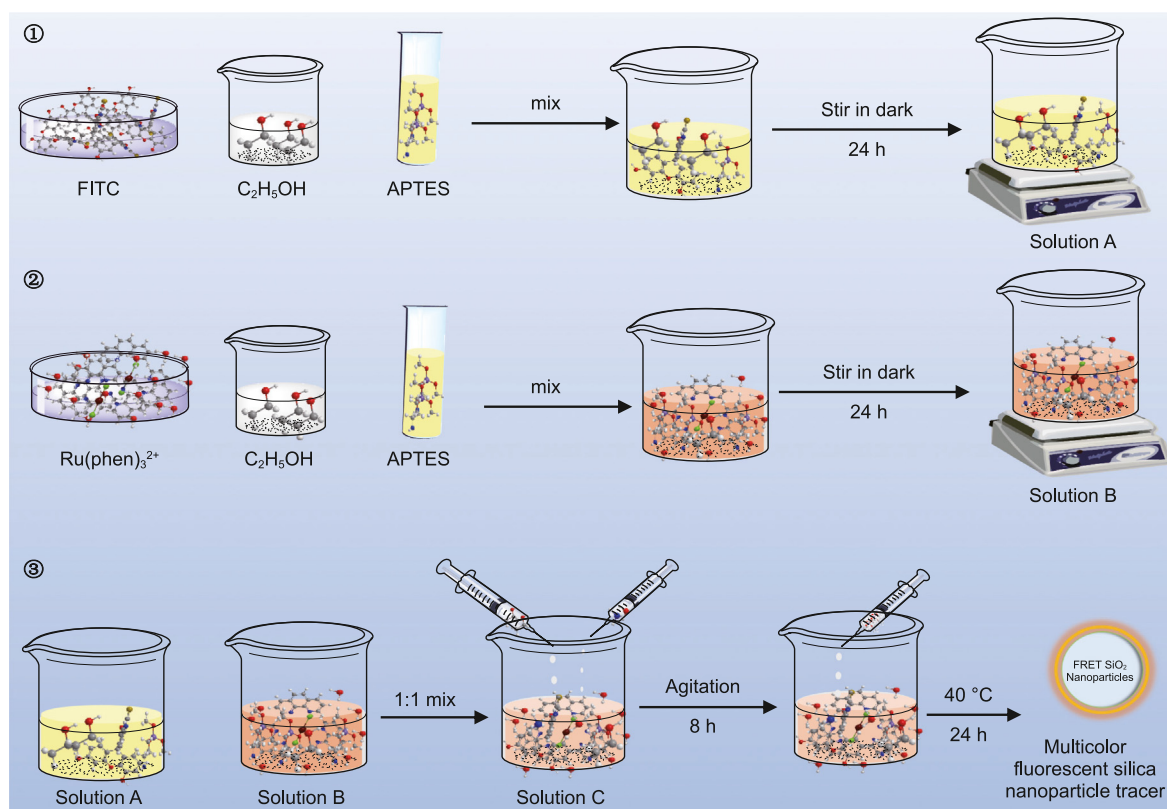


Fig. 1. Schematic of the fluorescent silica nanoparticle synthesis.

25, 40, and 80 °C for 160 h, with 2 mL samples collected every 2 h to measure the fluorescence intensity change. Because the temperature did not affect the zeta potential of the dispersion, only the dispersion concentration could be evaluated to determine the effect of temperature changes. Therefore, 2 mL of the dispersible solution supernatant was collected after 160 h at various experimental temperatures to test the concentration of the supernatant using the standard concentration curve method, and the change in concentration determined the influence of temperature on the dispersion.

2.5. Transport experiment of the FRET@SiO₂ nanoparticle tracer

2.5.1. Transport experimental apparatus

Fig. 2 shows a schematic of the tracer transport experimental equipment, which featured a constant-speed, constant-flow pump with maximum and minimum flow rates of 9.99 and 0.01 mL/min, respectively. The maximum pump pressure of the constant speed injection tracer was 20 MPa, and the pump pressure was set to 4 MPa in the experiment. The tracer concentration was kept constant throughout the injection process to ensure a stable contact time between the fluid and the core during the experiment. Two intermediate vessels were linked in parallel and controlled by two valves: one holding simulated formation water, which is prepared based on the composition of formation water from a certain oil field in the Bohai Sea. Deionized water is used to dissolve an appropriate amount of NaCl, and the pH is adjusted to between 6 and 8 by adding NaOH, and the other storing the solution of FRET@SiO₂ nanoparticle tracers. The pressure sensor inserted between the intermediate vessels and core holder monitored the real-time pressure of the fluid injection. The fluid input end of the core holder was connected in series with two intermediary vessels to install the experimental core and achieve fluid infusion. A fluid pump was connected to the core holder to fix the core. The core fluid flow normally percolates when the injection pressure is lower than the confining pressure. The outflow end of the core holder was attached to the collecting bottle, and the outflow fluid was quantitatively analyzed using a fluorescence spectrometer.

2.5.2. Preparation of the sandstone core

Two types of sandstone cores were used in this investigation. Natural sandstone cores were selected from the Bohai Oilfield, and

artificial sandstone cores were created using the same characteristics as the actual sandstone cores. A natural sandstone core was used to study the transport of fluorescent silica nanoparticles in a natural sandstone environment, which included the effects of pore throat size, clay minerals, and permeability. Artificial cores were used to study the transport characteristics of fluorescent silica nanoparticles in porous media under various injection parameters. Natural sandstone cores were prepared as follows before use: 1) The natural core was placed in the core oil cleaning apparatus to be treated for oil; 2) parameters (such as mass, length, and the radius of the section) of the dried core following oil cleaning were measured; 3) porosity and permeability of natural sandstone scores were measured using the high-temperature and high-pressure core multi-parameter instrument (SCMS-E); 4) pore-throat size distribution of natural sandstone cores was measured using a nuclear magnetic resonance instrument (MacroMR12-150H-I); 5) clay minerals in natural sandstone cores were measured using an X-ray diffractometer (X'Pert Pro); the natural sandstone cores were saturated with a 2000 mg/L sodium chloride solution, then subjected to vacuum treatment and stored for future use. Artificial cores were fabricated using the specifications of natural sandstone cores, with the grain size distribution selected to match that of authentic sandstone cores. After mixing a specified amount of skeleton particles with simulated formation water and stirring uniformly, a cementing agent was added. The resulting mixture was then placed into a pre-cleaned mold and compacted using a hydraulic press to form the artificial cores. Finally, after baking at 60 °C for 24 h, the cores were allowed to cool naturally to room temperature before being removed from the mold (Wang et al., 2019; Chang et al., 2018).

2.5.3. Transport properties in sandstone core

The transport and retention characteristics of fluorescent silica nanoparticles in sandstone cores were evaluated through 12 experiments. Three of these experiments focused on the transport behavior of the nanoparticles in three different natural sandstone environments and examined the impact of clay minerals on the retention of nanoparticles within the natural sandstone cores. The transport and retention characteristics of fluorescent silica nanoparticles were evaluated in 12 sets of artificial sandstone cores under different injection conditions, including nanoparticle size, concentration, salinity, and flow velocity. Briefly, the experimental

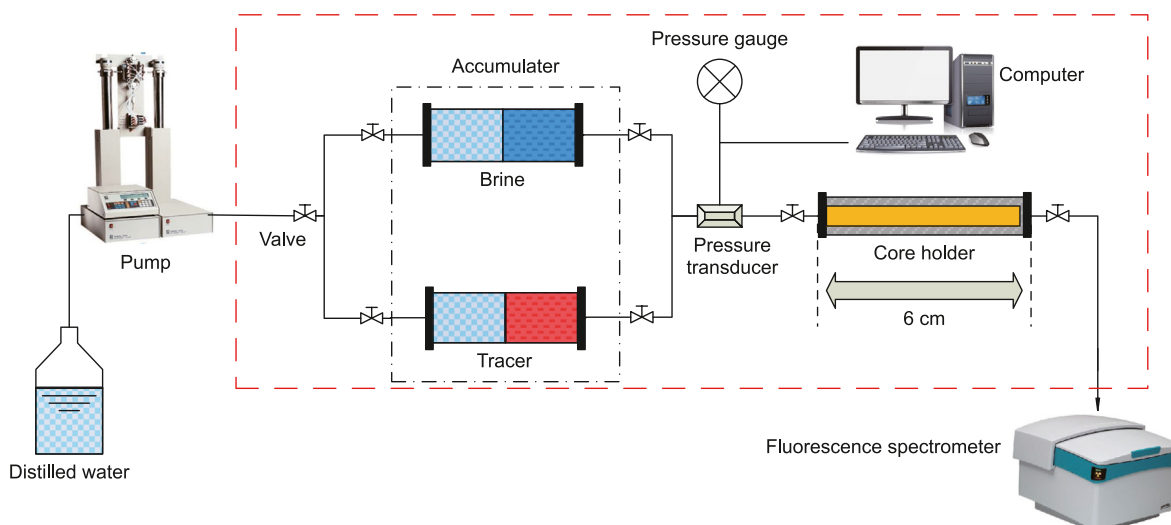


Fig. 2. Schematic diagram of transport experimental apparatus.

cores were dried in a 60 °C incubator for 24 h. Subsequently, the dried cores were weighed and placed into a vacuum dish filled with saltwater to saturate for 12 h. The experimental core was placed in the core holder, and the confining pump pressure was adjusted to 4 MPa to secure it. The injection rate of the constant-flow pump was set to 2 mL/min, and 15–20 PV of saltwater was injected into the experimental core under the experimental conditions until the injection pressure was steady (PV is used to quantify the capacity of pore space. In this context, when used as a unit, it represents the amount of fluid that can be accommodated within the pores of a sandstone core as the fluid passes through it). The water-phase permeability of the experimental core was determined using Darcy's formula ($k = -Q\mu L/A\Delta P$), and the pressure at the time of stability was recorded. The pressure sensor is installed between the intermediate container and the core holder and is responsible for recording the real-time pressure during fluid injection. Subsequently, the core holder was connected to the intermediate container containing fluorescent silica nanoparticles, and 2.5 PV fluorescent silica nanoparticles were pumped into the experimental core at a flow rate of 0.5 mL/min, followed by 2.5 mL brine at the same flow rate (the injectate was not subjected to any special treatment or deoxygenation before use). This velocity equates to a pore–water velocity of 2.56 m/d and translates to a core residence time of 0.25 h and Reynolds number of 0.0186, which is orders of magnitude less than the core limit ($Re \leq 10$).

Displacement fluid was collected at the outflow end of the core holder and at 0.1 PV intervals. The concentration was measured using a fluorescence spectrometer and the collected displacement solution. The excitation wavelength was 450 nm, and the slit width was 2.5 nm. The emission wavelength of the fluorescent silica nanoparticles ranges from 300 to 700 nm, with a maximum emission wavelength of around 576 nm, respectively. After each core flow experiment, the core was initially rinsed with deionized water to remove any residual fluorescent silica nanoparticles, followed by 40 min of ultrasonic treatment to further eliminate the nanoparticles. Table 1 summarizes the experimental conditions of the 19 experiments.

2.5.4. Quantitative detection method based on fluorescence intensity

A fluorescence spectrometer was used to quantitatively detect the displacement fluid in this study, and every 0.1 PV of displacement fluid was recorded as a sampling unit and placed in the sample bottle. The quantitative detection method based on fluorescence intensity primarily evaluates the maximum fluorescence intensity of the standard liquid solution to be tested. The unknown sample concentration was calculated using the F-C diagram of engagement and maximum fluorescence intensity. The following

are certain examples of specific methods: standard solutions of 10, 50, 100, 200, and 500 mg/L were used to determine the maximum fluorescence intensity under the same conditions (excitation wavelength and slit width), the relationship between fluorescence intensity and concentration was determined, and functional relationship between the two by fitting was obtained. The fluorescence spectra of 50 samples were evaluated after each experiment to determine the maximum fluorescence intensity of each sample, which was then used to compute the concentration.

3. Results and discussion

3.1. Characterization of the FRET@SiO₂ nanoparticle tracer

3.1.1. Fourier-transform infrared (FT-IR) spectroscopy

In this study, multicolor fluorescent silica nanoparticle tracers based on FRET were synthesized via a sol-gel process using ammonia and water as catalysts following a modified Stöber synthesis method. The structure of the synthesized fluorescent silica nanoparticle tracer was characterized using FT-IR spectroscopy.

Fig. 3 shows the FT-IR spectra of the synthesized fluorescent silica nanoparticle tracer and conventional silica particles. The

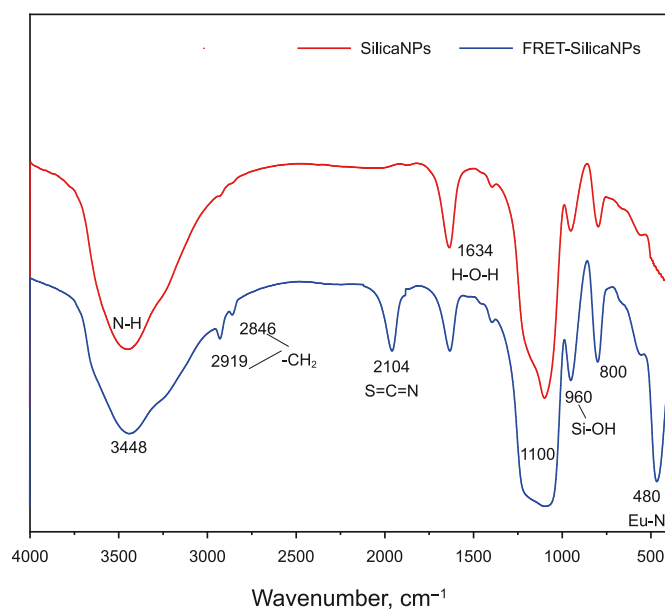


Fig. 3. FT-IR spectra of the synthesized FRET@SiO₂ nanoparticle tracer and original silica nanoparticles.

Table 1

Experimental conditions for the fluorescent silica nanoparticle transport studies conducted on natural sandstone and artificial cores.

Type	Exp.	Flow rate, mL/min	Porosity, %	Permeability, md	Pore volume, cm ³	Particle size, nm	Concentration, mg/L	Salinity, mg/L	Temperature, °C	Clay minerals
Natural core	N1	0.5	10.9	717	2.97	50	10	1000	25	yes
	N2	0.5	11.1	440	2.12	50	10	1000	25	yes
	N3	0.5	12.1	386	2.02	50	10	1000	25	yes
Artificial core	A1	0.5	15.5	365	4.97	50	10	1000	25	no
	A2	0.2	13.6	401	4.12	50	10	1000	25	no
	A3	1	14.1	389	4.28	50	10	1000	25	no
	A4	0.5	13.6	377	4.12	100	10	1000	25	no
	A5	0.5	14	356	4.24	200	10	1000	25	no
	A6	0.5	15.6	345	4.73	50	10	5000	25	no
	A7	0.5	15	417	4.55	50	10	10000	25	no
	A8	0.5	13.9	396	4.21	50	20	1000	25	no
	A9	0.5	15.1	378	4.58	50	30	1000	25	no

synthesized FRET@SiO₂ nano-tracer exhibited typical stretching vibration absorption peaks of Si–O–Si at 800 and 1100 cm⁻¹. Moreover, stretching vibration absorption peaks of Si–OH and –OH, as well as the bending vibration absorption peak of H–O–H were observed at 960, 3478, and 1634 cm⁻¹, respectively. The absorption peak appeared because the water adsorbed by the FRET@SiO₂ nano-tracer was not entirely removed, and condensation between the hydroxyl groups caused the FRET@SiO₂ nano-tracer to agglomerate to form Si–O–Si. In addition, compared to the original silica nanoparticles, the FRET@SiO₂ nano-tracer had a stretching vibration absorption band of N–H at 3400 cm⁻¹. The FRET@SiO₂ nano-tracer had stretching vibration absorption bands of –CH₂ at 2919 and 2846 cm⁻¹, indicating that the functional groups in the silane coupling agent were successfully grafted onto the surface of the silica nanoparticles. The stretching vibration peak (–S=C=N) in FITC was at 2104 cm⁻¹. The Eu–N-stretching vibration peak in Ru(phen₃)²⁺ appeared at 470 cm⁻¹. Based on the spectrum functional group analysis, the multi-color fluorescent nano-tracer was successfully synthesized.

3.1.2. Ultraviolet absorption wavelength and fluorescence spectrum

The emission spectra and luminescence characteristics of the synthesized fluorescent silica nanoparticle tracers at the maximum absorption wavelength were obtained using UV and fluorescence spectroscopies.

Fig. 4 shows that the fluorescent silica nanoparticle tracer exhibits the strongest absorption in the UV-Vis region, with absorption wavelengths ranging from 300 to 700 nm. A pronounced absorption peak occurs at 450 nm, within the transition from ultraviolet to visible light, and a weak absorption peak is observed at 500 nm. Fig. 5 shows the fluorescence emission spectra of the FITC@SiO₂, Ru(phen₃)²⁺@SiO₂, and FRET@SiO₂ nanoparticle tracers excited at a wavelength of 450 nm with a slit width of 1 nm. Experimental results revealed that under the same excitation wavelength, the maximum peak wavelengths of the FITC@SiO₂ and Ru(phen₃)²⁺@SiO₂ nanoparticle tracers were 520 and 576 nm, respectively, and their emission spectra have a specific overlap region. The emission spectra of the FRET@SiO₂ nanoparticle tracer had peaks at 520 and 576 nm, and the maximum peak was higher than that of the single dye, suggesting that the energy transfer of FITC and Ru(phen₃)²⁺ enhanced the fluorescence intensity of the

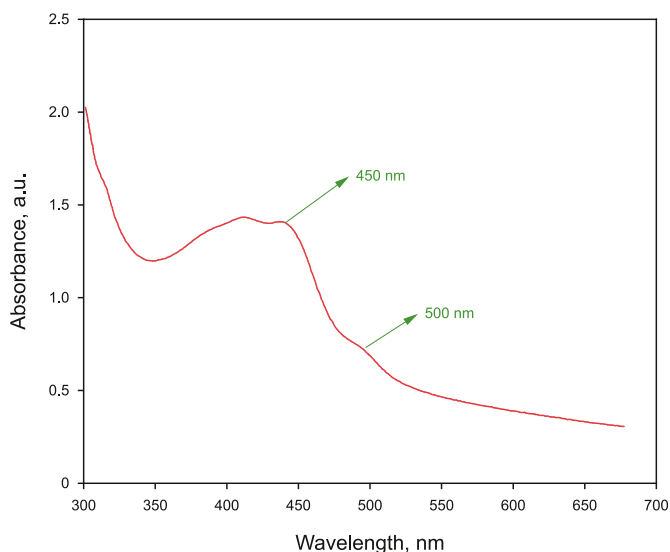


Fig. 4. Ultraviolet absorption spectrum of the FRET@SiO₂ nanoparticle tracer (300–700 nm).

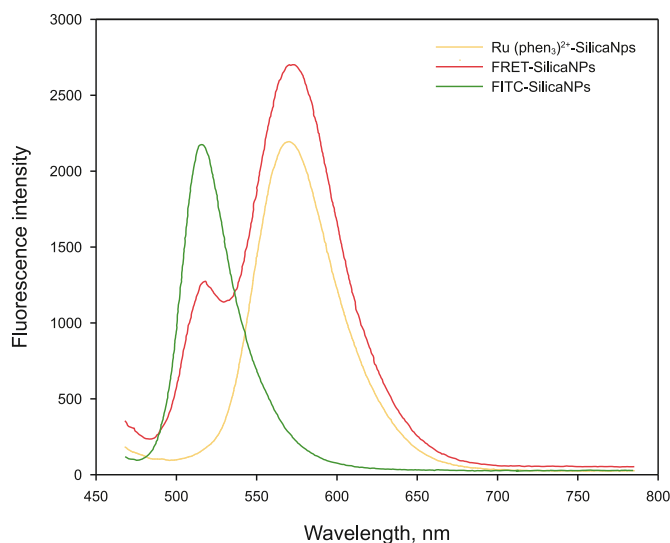


Fig. 5. Fluorescence emission spectra of the FRET@SiO₂ nanoparticle tracer (excitation wavelength: 450 nm; slit width: 1 nm).

fluorescent silica nanoparticles.

3.1.3. Morphology analysis

Field-emission scanning electron microscopy was used to observe the appearance and size of the synthesized FRET@SiO₂ nano-tracer and SiO₂ nanoparticles. The FRET@SiO₂ nano-tracer and SiO₂ nanoparticles (1 mg) were added to 100 mL of absolute ethanol and ultrasonically dispersed for 40 min. A small amount of the upper dispersed droplets was drawn into a copper sample coated with conductive adhesive using a rubber head dropper. Subsequently, the sample was naturally dried, gilded, and placed under an electron microscope to observe its appearance, size, and dispersion. Field emission electron microscopy images of the FRET@SiO₂ nano-tracer and SiO₂ nanoparticles are shown in Fig. 6, which reveal uniform spheres and similar particle sizes of 50 ± 5 nm.

3.1.4. Particle size distribution

The synthesized FRET@SiO₂ nano-tracer and SiO₂ nanoparticles (0.05 mL) were placed into a glass spiral sample bottle, and deionized water was added to dilute the solution to 50 mL to obtain a 10 mg/L clear and transparent diluent. The particle size distribution was then measured. Fig. 7 shows the particle size distribution of 50 mg/L of the FRET@SiO₂ nano-tracer and SiO₂ nanoparticle deionized water dispersion using a laser particle size analyzer, with a shading rate of 3.48%. The median average particle sizes (D50) of the SiO₂ nanoparticles and FRET@SiO₂ nano-tracers were 52.3 and 55.18 nm, respectively. Grafting FITC and Ru complexes onto the surface of SiO₂ nanoparticles slightly increased the particle size. However, the increase was insignificant and did not affect the excellent migration characteristics of nano-silica in the reservoir. The uniform particle size distribution of the tracer is consistent with the morphological results shown in Fig. 6. In addition, the uniform particle size distribution indicated that the FRET@SiO₂ nano-tracer had good dispersibility in deionized water.

3.2. Mechanism of FRET in fluorescent silica nanoparticle tracers

FRET refers to two different fluorescent groups: donor (D) and acceptor (A). In this study, FITC was selected as the donor, and Ru(phen₃)²⁺ was used as the acceptor. If the emission spectrum of

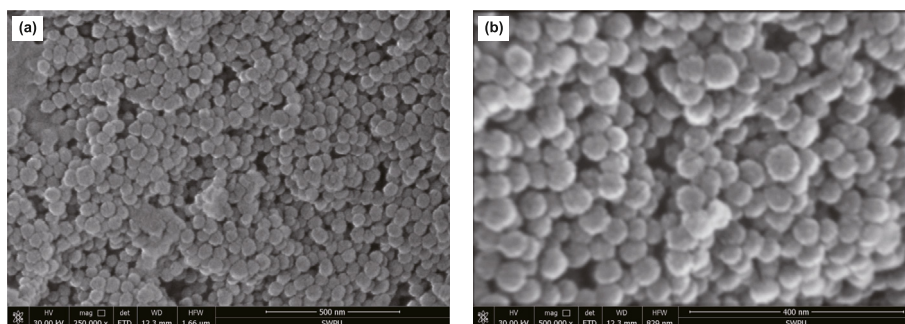


Fig. 6. Micro-morphology of the FRET@SiO₂ nano-tracer and SiO₂ nanoparticles. (a) FRET@SiO₂ nano-tracers and (b) SiO₂ nanoparticles at a magnification of 500000×.

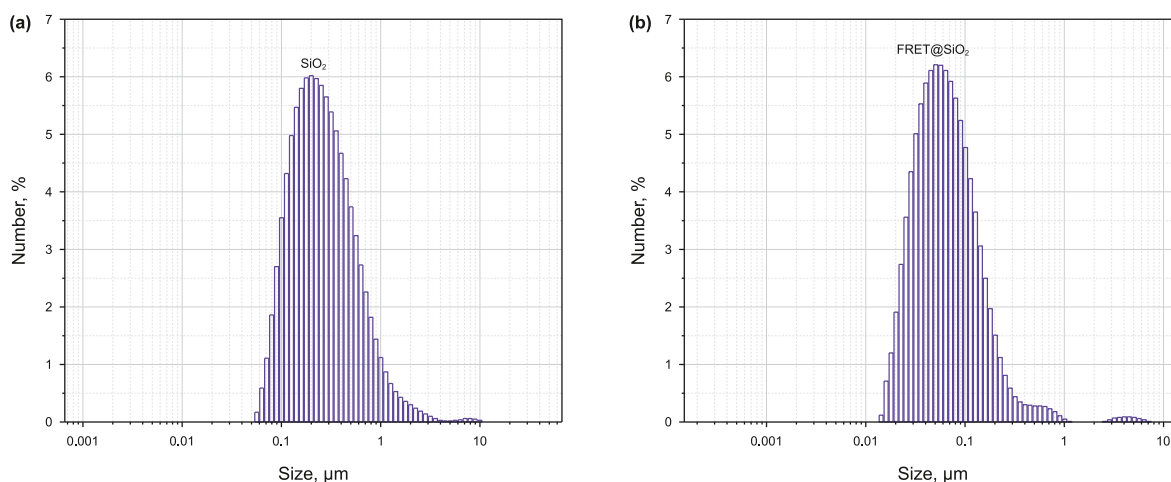


Fig. 7. Particle size distributions of the SiO₂ nanoparticles and FRET@SiO₂ nano-tracers.

the donor can effectively overlap with the excitation spectrum of the acceptor and the distance between the two is between 1.0 and 10 nm, the phenomenon of energy transfer from the donor to the acceptor can be observed when the excitation light of the donor is used (Murugesan et al., 2020).

Fig. 8(a) shows the fluorescence emission spectra of the FITC and FITC monochrome fluorescent nano-tracer at an excitation wavelength of 450 nm. Fig. 8(b) shows the fluorescence excitation spectra of the Ru(phen₃)²⁺ and Ru(phen₃)²⁺ monochrome

fluorescent nano-tracer at an excitation wavelength of 518 nm. The emission wavelength of FITC was 518 nm, and the excitation wavelength of Ru(phen₃)²⁺ was 510 nm. The distance between the two was between 1.0 and 10 nm when using the excitation light of the donor FITC. Moreover, energy transfer phenomenon could be observed from the donor FITC to the receptor Ru(phen₃)²⁺.

After the donor molecule is excited by the source, it transitions from the ground state to the excited state, which produces an oscillating dipole during the secondary process. The oscillating

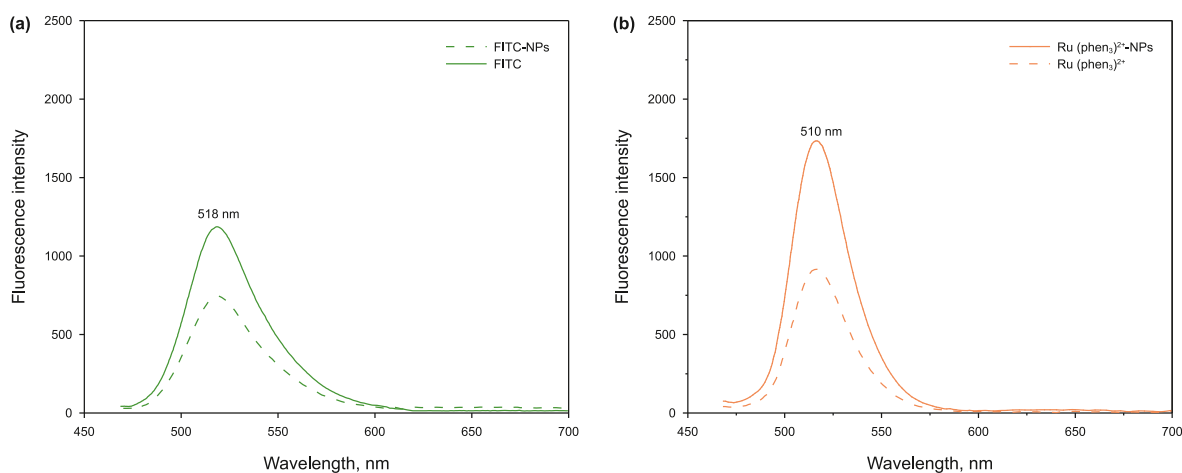


Fig. 8. Excitation wavelength of Ru(phen₃)²⁺ and emission wavelength of FITC.

dipole of the donor molecule can resonate with the dipole of a nearby recipient molecule. Owing to the dipole-dipole interaction, the donor molecule that is in the excited state can transfer some or all of its energy to the acceptor via a nonradiative transition, thus causing the acceptor molecule to become excited. During this process, the fluorescence intensity of the donor molecule decreases, whereas that of the acceptor molecule increases. The rate of energy transfer from an energy donor to an energy acceptor depends on the sixth power of distance (Dhir and Datta, 2016).

$$k_{ET} = \frac{1}{\tau_D} \left(\frac{R_0}{R} \right)^6$$

where, τ_D is the lifetime of the energy donor without the energy receptor, and R_0 is the constant of the donor-acceptor pair- Förster radius.

FRET typically occurs at a distance of a few nanometers and only when the donor and acceptor are physically connected. The generated energy excites the acceptor molecule at different concentrations when the donor molecule is excited at a particular wavelength. By adjusting the composition and concentration of the receptor, a multicolor fluorescent silica nanoparticle tracer can be produced by utilizing the energy transfer of the donor molecule. Fig. 9 shows the emission spectrum of the FRET-fluorescent silica nanoparticles synthesized by adding two fluorescent dyes with different molar ratios under an excitation wavelength of 450 nm. The emission spectrum peaks of the three fluorescent silica nanoparticles were entirely different. When FITC: Ru(phen₃)²⁺ < 1:1, the peak height of the FRET fluorescent silica nanoparticles at 576 nm was more significant than that at 520 nm. Conversely, when the ratio was > 1:1, the peak height at 576 nm was less than that at 520 nm.

When FITC was excited by a light source, the energy was transferred to Ru(phen₃)²⁺ via a nonradiative transition. Therefore, the fluorescence intensity of Ru(phen₃)²⁺ increased and a short blue shift occurred. The ratio of the two fluorescent dyes directly affected the fluorescence characteristics of the tracer. Energy transfer was achieved when the ratio of FITC-to-Ru(phen₃)²⁺ attained a certain level (1:1). The higher the ratio of Ru(phen₃)²⁺, the greater is the energy transfer and higher the peak height. In addition, by adjusting the composition and ratio of the energy

donor and acceptor, multicolor fluorescent nano-tracers with enhanced fluorescence characteristics could be prepared using the energy transfer of the donor molecule, and the tracers synthesized at each ratio exhibit unique fluorescence characteristics. Therefore, the types of fluorescent tracers available could be further expanded.

3.3. Quantitative detection of the FRET@SiO₂ nanoparticle tracer based on fluorescence intensity

The fluorescence quantitative detection method offers advantages over the traditional absorbance quantitative detection method (Lee et al., 2022; Wang et al., 2023; Yang et al., 2021). These advantages include a sensitivity of approximately 1000 times that of absorbance spectrophotometry and the elimination of non-fluorescence impurities because only fluorescent molecules can be detected under specific wavelength excitation. Furthermore, this method is accurate up to five orders of magnitude of concentration, thus removing the requirement for sample dilution or other treatments and saving time in the laboratory. In this study, a fluorescence approach was used to quantify the concentration of the FRET@SiO₂ nanoparticle tracer. Table 2 lists the test parameters for various FRET@SiO₂ nanoparticle tracer concentrations, and Fig. 10 depicts the linear connection between FRET@SiO₂ nanoparticle tracer concentration and the maximum fluorescence intensity. Under the same test settings, the tracer concentration had an excellent linear relationship with the maximum fluorescence intensity of the energy acceptor Ru(phen₃)²⁺, with a functional relationship of $y = 6.7109x$ ($R^2 = 0.9828$) that can be used for the quantitative detection of unknown solution concentrations.

3.4. Stability of the FRET@SiO₂ nanoparticle tracer in reservoir environments

3.4.1. Effect of temperature on stability of FRET@SiO₂ nanoparticle tracer

Reservoir conditions are typically harsh, with temperatures exceeding 65 °C and salinities reaching up to 100,000 mg/L or higher. These characteristics affect the dispersion and fluorescence stability of the FRET@SiO₂ nanoparticle tracer in the injected medium. Thus, it was critical to evaluate the adaptation of the FRET@SiO₂ nanoparticle tracer to a reservoir environment. Zeta potential refers to the electrical potential difference between particle surfaces and the surrounding liquid, reflecting charge distribution. It plays a key role in particle stability, dispersion, and interactions. In this study, we measured Zeta potential via electrophoretic light scattering and observed an increase from −38.29 to −33.06 mV as temperature increased at neutral pH. Although we did not measure the Zeta potential of sandstone surfaces directly, existing literature indicates they typically carry a negative charge at neutral pH, which may affect tracer adsorption and migration. Fig. 11 shows that after placing 50 mg/L FRET@SiO₂ nanoparticle tracers in deionized water at seven different temperatures (25, 35, 45, 55, 65, 75, and 85 °C) for 160 h, the concentrations of the seven groups of dispersion decreased to 46.57, 45.86, 44.67, 43.56, 41.45, 37.97 and 35.58 mg/L, respectively, and the initial zeta potential of the dispersion is −38.29 mV. After the experiment, the zeta potentials increased. Therefore, the stability of the FRET@SiO₂ nanoparticle tracer dispersion solution decreased with increasing temperature. According to the DLVO theory of solution stability, when the temperature increases, the Brownian movement of particles in the dispersed solution also increases. Moreover, the energy of collisions between particles may cross the energy barrier between the dispersed and stable particles, thus reducing the space between particles and causing particle settlement. Although the

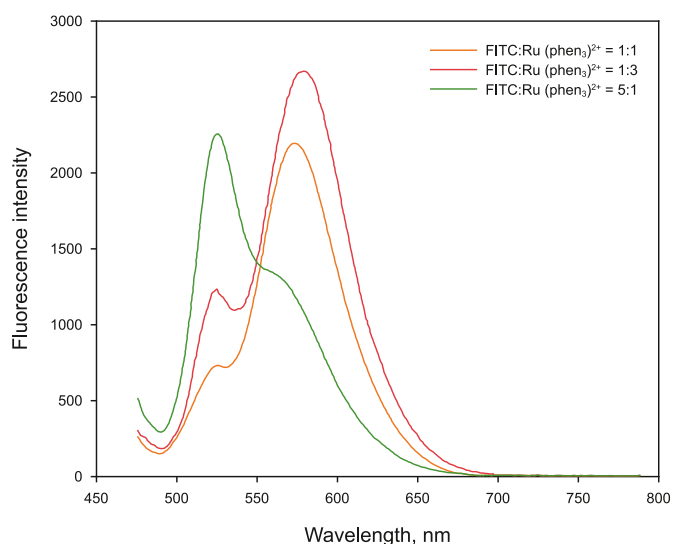


Fig. 9. Fluorescence emission spectra of FRET@SiO₂ nanoparticle tracers synthesized using different molar ratios of two fluorescent monomers.

Table 2
Test parameters of a fluorescence spectrometer.

Concentration, mg/L	Start, nm	Apex, nm	End, nm	Height, Data	EX slit, nm	EM slit, nm	Scan speed, nm/min	EX wavelength, nm
50	465.6	518.4	710.0	382.2	1.0	2.5	240.0	450.0
100	461.4	519.6	662.6	776.9	1.0	2.5	240.0	450.0
150	455.8	521.4	678.8	1089.0	1.0	2.5	240.0	450.0
200	467.6	522.4	678.8	1343.0	1.0	2.5	240.0	450.0
250	463.8	525.4	692.0	1576.0	1.0	2.5	240.0	450.0

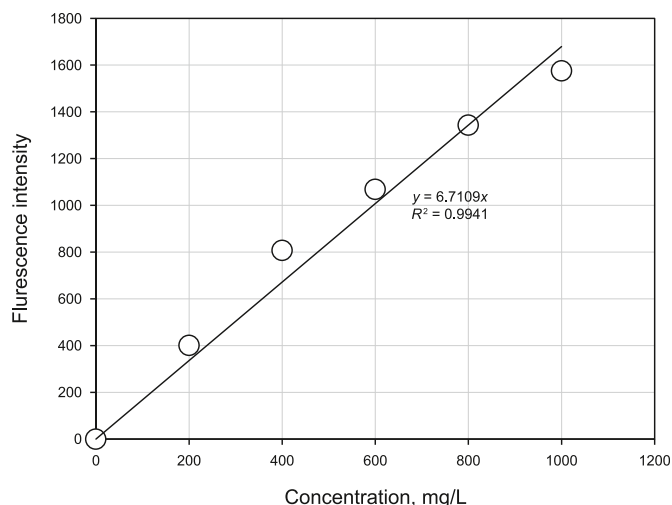


Fig. 10. Linear relationship between concentration and fluorescence intensity of the FRET@SiO₂ nanoparticle tracer.

stability of the FRET@SiO₂ nanoparticle tracer dispersion solution decreased as the temperature increased, the zeta potential of the FRET@SiO₂ nanoparticle tracer dispersion solution was -33.06 mV at a reservoir temperature of 85 °C, demonstrating its high dispersion capability. This also indicates that no large-scale particle aggregation or sedimentation occurred during the injection of the fluorescent silica nanoparticles.

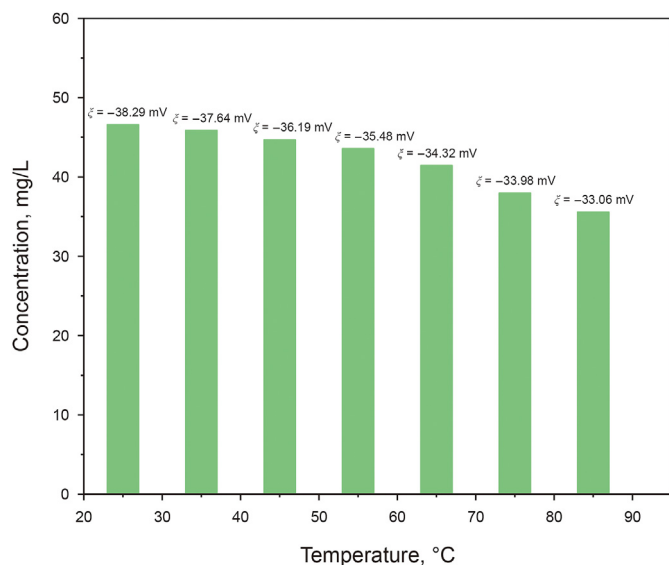


Fig. 11. Dispersion concentrations of the FRET@SiO₂ nanoparticle tracer at different temperatures (standing time: 160 h).

3.4.2. The effect of salinity on the stability of FRET@SiO₂ nanoparticle tracers

Fig. 12(a) shows the variation in fluorescence intensity over time for the three groups of FRET@SiO₂ nanoparticle tracer dispersions at different temperatures. After resting at 65 °C for 160 h, the fluorescence intensity of the fluorescent silica nanoparticle dispersions minimally changed, indicating good fluorescence stability. As the experimental temperature increased, the fluorescence intensity of the dispersion solution tended to stabilize after gradually decreasing with standing time. Moreover, the fluorescence intensity decreased with increasing temperature. This phenomenon was primarily caused by Ru(phen₃)²⁺ in the FRET@SiO₂ nanoparticle tracer. There are three types of electron transitions in Ru(phen₃)²⁺: 1) metal-to-ligand charge-transfer excited state (MLCT) with electrons from the π M metal orbital to π L* ligand orbital; 2) metal-center excited state with electrons from the π M orbital to π M* orbital; and 3) ligand-center excited state with electrons from the π L orbital to π L* orbital. Owing to its relatively large spin-orbit coupling effect, the 3MLCT excited state has a higher radiation inactivation rate constant, making it easier to emit light in an average- or high-temperature solution system. If the temperature increases, the excited-state lifetime of 3MLCT decreases, and the corresponding luminescence intensity also decreases. Therefore, the fluorescence intensity of the dispersion solution of the FRET@SiO₂ nanoparticle tracer exhibited temperature sensitivity. Fig. 12(b) shows the linear relationship between temperature and the fluorescence intensity.

Fig. 13 presents the experimental results of the dispersion stability and fluorescence stability of the FRET@SiO₂ nanoparticle tracer in solutions with different salinities. During the experiment, the temperature of the dispersion was maintained at 65 °C. As shown in the figure, with the increase in salinity, the Zeta potential of the FRET@SiO₂ nanoparticle tracer dispersion also increases. After 160 h, the zeta potentials of the four groups of FRET@SiO₂ nanoparticle tracer dispersions were -36.1 , -27 , -19.6 , and -12.4 mV. Due to the influence of double-layer repulsive force, the higher the absolute value of the potential (ξ) of the dispersion solution, the better the dispersion of the solution. Based on the experimental results, the dispersion solution had a high dispersion performance in NaCl solutions <5000 mg/L but poor dispersion performance at $10,000$ mg/L. The effect of salinity on the stability of the FRET@SiO₂ nanoparticle tracer dispersion solution can be regarded as the action of charged ions. With the addition of the electrolyte, the total concentration of positively charged ions in the dispersed liquid system increased. This phenomenon increased the possibility that the particles attracted counter-ions and caused more diffuse counter-ions to enter the adsorption layer, thereby reducing the absolute value of the zeta potential of the diffusion double layer. The dispersion achieved an isoelectric state and lost stability when the quantities of positive and negative charges in the adsorption layer were equal, and the zeta potential decreased to zero. Therefore, the effect of electrolytes on the dispersion of functional nanoparticles was due to charge-neutralization.

Fig. 13(b) shows the change in fluorescence intensity of the

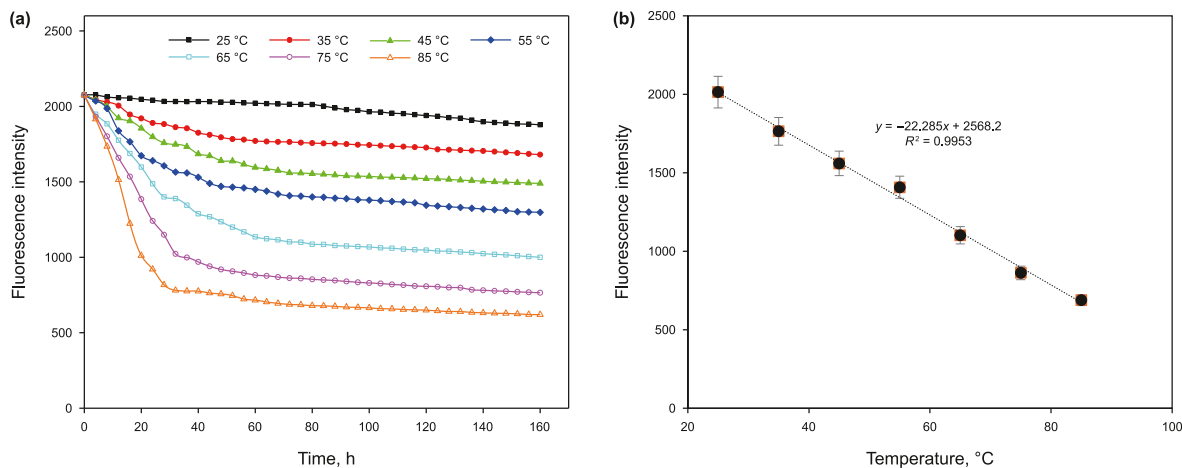


Fig. 12. (a) Fluorescence intensity of the FRET@SiO₂ nanoparticle tracer varied with time at different temperatures. (b) The linear relationship between temperature and fluorescence intensity of the FRET@SiO₂ nanoparticle tracer.

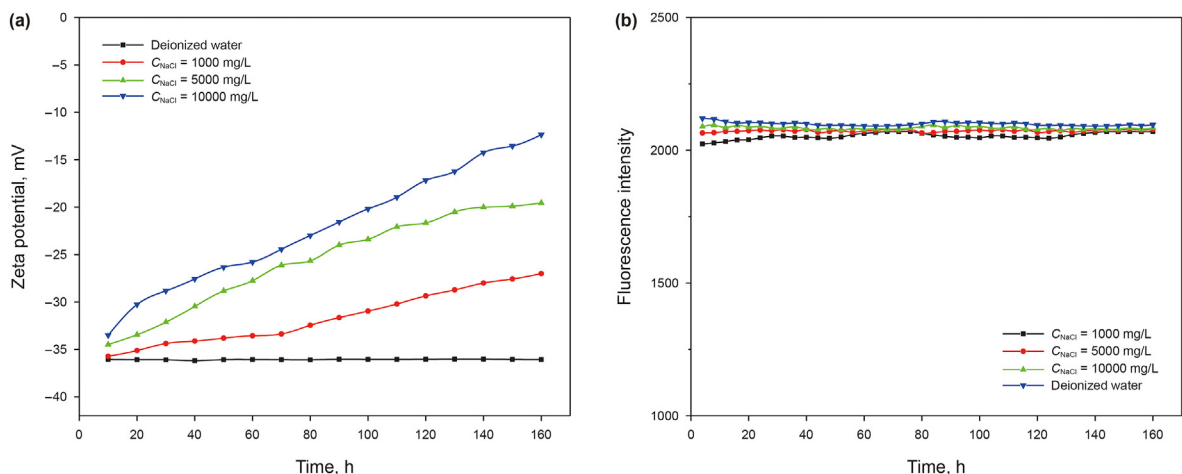


Fig. 13. (a) Zeta potential curve and (b) fluorescence intensity of the FRET@SiO₂ nanoparticle tracer varying with time at different salinities.

dispersion solution at different salinity levels. To avoid fluorescence intensity changes caused by concentration changes in the dispersion solution settlement, each sample was ultrasonicated for 20 min before testing to consider the single effect of salinity on fluorescence intensity. The experimental results indicate that, initially, the fluorescence nanoparticles disperse well in deionized water, exhibiting high fluorescence intensity. However, over time, the particles slightly aggregate, leading to a decrease in fluorescence signal, which then increases again once the aggregates stabilize. Throughout the process, changes in fluorescence intensity are minimal and can be considered experimental noise or incidental fluctuations. In NaCl solution, the fluorescence intensity first shows a slight increase, then stabilizes, with overall changes being minimal. This phenomenon is primarily due to initial measurement errors, which are smoothed out with repeated experiments, resulting in a stable fluorescence intensity.

3.4.3. The interaction effect of temperature and salinity on the stability of FRET@SiO₂ nanoparticle tracers

Fig. 14 shows the changes in fluorescence intensity and zeta potential of the fluorescent nanoparticle tracer dispersion after 160 h at high temperature (90–150 °C) and high salinity (12000–20000 mg/L). As shown in the figure, with increasing

temperature and salinity, the fluorescence intensity decreases, zeta potential increases, and the dispersion stability deteriorates. The analysis indicates that as the electrolyte concentration increases, the total concentration of charge ions in the system rises. At the same time, the increase in temperature enhances the thermal motion of electrolyte molecules, causing more diffusing ions to enter the adsorption layer. This reduces the absolute value of the zeta potential of the diffuse double layer, thereby decreasing the stability of the dispersion and lowering the fluorescence intensity. When the zeta potential approaches zero, the dispersion loses its stability. However, during the experiment, even when the temperature reached 150 °C and salinity reached 20000 mg/L, the zeta potential remained negative. Therefore, the dispersion is stable and suitable for use under reservoir conditions (150 °C, 20000 mg/L salinity).

3.5. Transport characteristics of the FRET@SiO₂ nanoparticle tracer in sandstone cores

3.5.1. Effects of sensitive clay minerals on transport and retention

Compared to quartz sand-packed columns and artificial cores, the key characteristic of natural cores is the presence of various sensitive clay minerals. Sensitive clay minerals in sandstone

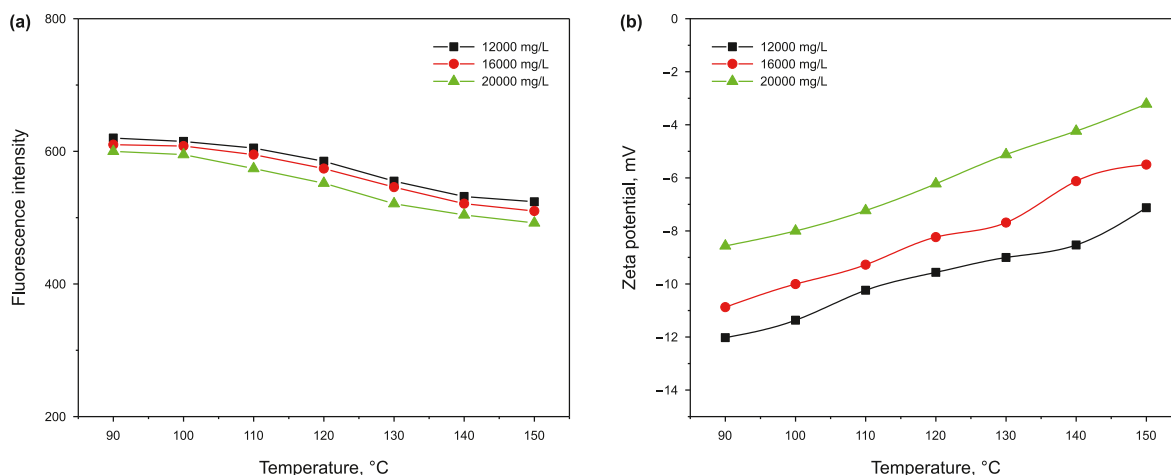


Fig. 14. Zeta potential (a) and fluorescence intensity (b) changes of FRET@SiO₂ nanoparticle tracer under the interaction of temperature and salinity.

reservoirs primarily include kaolinite, montmorillonite, chlorite, and illite, and the characteristics of these clay minerals affect fluid transport in porous media. Fig. 15 shows the X-ray diffraction patterns of three natural sandstone cores. The significant components of sandstone are quartz and albite, comprising approximately 70%–90%. The clay minerals in the three selected natural cores differed. For example, core N1 contained only kaolinite, whereas cores N2 and N3 contained all clay minerals. Table 3 lists the relative contents of each component in the three cores. In the three cores, kaolin accounted for approximately 4%–6% of the total rock composition. The N2 and N3 montmorillonite contents were 3.07% and 7.17%, chlorite contents were 9.78% and 16.28%, and illite contents were 2.18% and 3.26%, respectively. The sensitive clay weights of the three cores (N1, N2, and N3) were 4.11%, 18.34%, and 28.74%, respectively.

Fig. 16 shows the zeta potential changes of sensitive clay minerals, rocks, and the FRET@SiO₂ nanoparticle tracers at different pH levels. The zeta potentials of all three compounds were negative at the experimental pH, indicating that they had similar surface characteristics. According to the double-layer repulsion theory, an electrostatic attraction is generated between the negatively charged FRET@SiO₂ nanoparticle tracer and positive ions in the fluid, thereby forming diffusion layers around the rock pore walls of particles and clay minerals. Thus, diffusion layers with similar charges overlap, creating an electric double-layer repulsion between the surfaces (Shiratori et al., 2009). These experimental results indicate that the self-charged nature of clay minerals is not conducive to particle adsorption and retention. However, in sensitive clay minerals, exchangeable cations in clay dissociate in water after fluid injection to form a diffusion double electric layer, which negatively charges the surface of the flake structure. Owing to electrostatic repulsion, the negatively charged sheet structure separates and causes clay expansion, which results in a narrow pore-throat channel for the migration of the FRET@SiO₂ nanoparticle tracers, causing the particles to accumulate at the pore throat and increasing the particle retention rate.

Fig. 17 shows the breakthrough curve and final retention rate of the FRET@SiO₂ nanoparticle tracer transported in the three natural core species. A FRET@SiO₂ nanoparticle tracer with a salinity of 1000 mg/L was injected into the natural cores. During injection, the relative concentration of particles (C/C_0) rapidly increased to a maximum, remained stable, and then quickly decreased to zero during displacement. According to Table 3, the clay mineral contents of the three natural cores were somewhat different ($N1 < N2 < N3$); therefore, the three cores had different degrees of

hydration expansion during the fluid injection process. Fig. 17 shows that the maximum relative concentrations in the three cores during injection decreased with an increase in clay minerals. The maximum relative concentrations in the three cores were 0.86 (2.15 PV), 0.72 (1.8 PV), and 0.71 (1.78 PV). Compared with cores N2 and N3, the relative concentration of the N1 core more quickly reduced to near zero, which indicates that clay hydration expansion changed the fluorescent silica nanoparticle transport corridor. In addition, this phenomenon resulted in a higher concentration of silica nanoparticles that were stranded in the core. The three core particle retention rates were 7.2%, 11.2%, and 11.9% for N1, N2, and N3, respectively.

3.5.2. Effects of nanoparticle size on transport and retention

The size of the tracer particle affects the matching connection between the tracer particle size and the pore-throat size, which is an essential factor in determining transport. When the particle size is $< 1/7$ of the pore throat size ($dP/dN > 1/7$), all the particles can freely pass through the pore throat. When the particle size is $1/7$ – $1/3$ of the pore throat size ($1/7 < dP/dN < 1/3$), most particles can enter the pore throat; however, certain particles accumulate outside, thus increasing the retention of particles. When the particle size is $> 1/3$ of the pore-throat size ($dP/dN < 1/3$), most particles cannot enter the pore throat and accumulate outside (Haider et al., 2021). Fig. 18 shows the nuclear magnetic resonance spectroscopy results for the pore-throat distribution of experimental core N1. The D50 of the pore throat of the core, which reflects its median diameter, was 1.23 μm . The sizes of the 50, 100, and 200 nanoparticles were generated by altering the quantity of ammonia in the catalyst during the production of the FRET@SiO₂ nanoparticle tracer. The particle size ratios (γ) between the three FRET@SiO₂ nanoparticle tracers and pore throat size were 0.041, 0.082, and 0.162.

Fig. 19 shows the breakthrough curves of the FRET@SiO₂ nanoparticle tracers with three core particle sizes. As the particle size increased, the maximum relative concentration of the output decreased. In contrast, retention rates for the three cores being 4.23%, 5.31%, and 9.84%, the maximum relative concentrations for the three cores were 0.96 (2.4 PV), 0.90 (2.28 PV), and 0.86 (2.13 PV), respectively. As the particle size increased, the particle accumulation at the pore throat increased, and the initial transport channel of the particles changed, thereby increasing the retention rate. Furthermore, the ratio of the particle size to the pore radius injected into the A5 core was 0.162, which was between $1/7$ and $1/3$. Most of the particles could enter the pores, but some of the

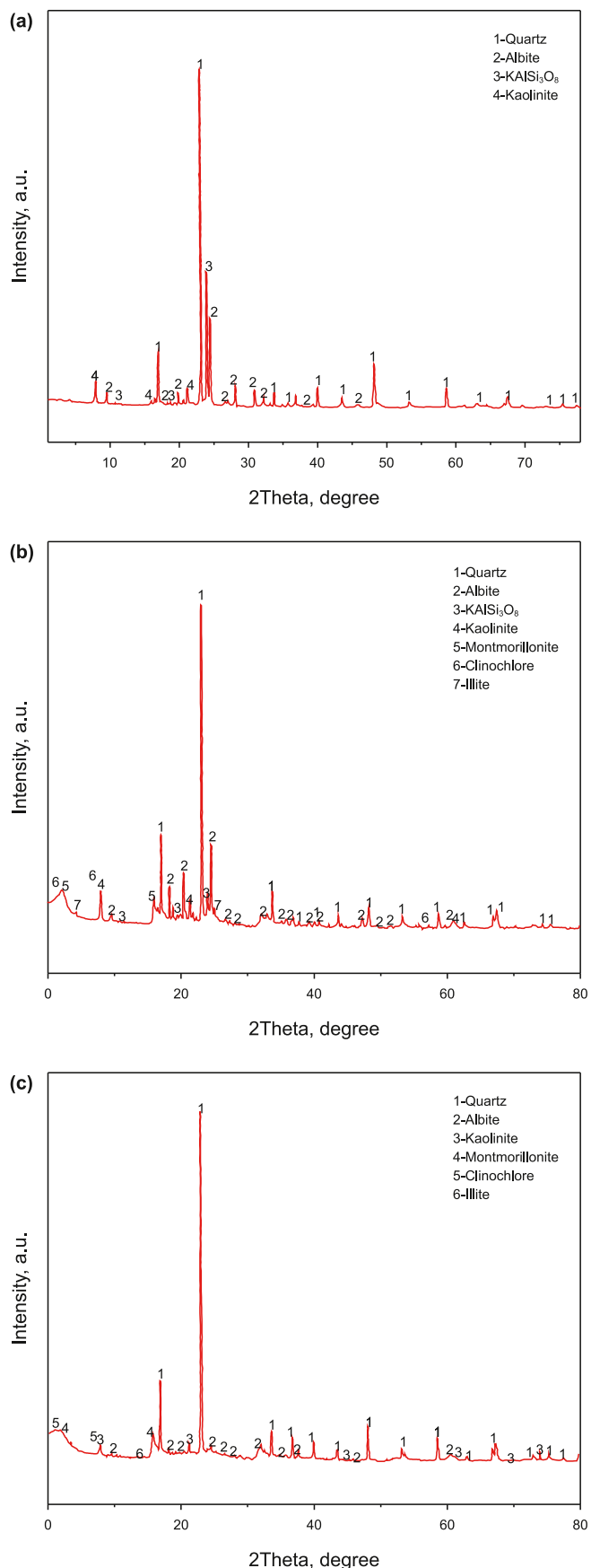


Fig. 15. X-ray diffraction patterns of sensitive clay minerals in three natural cores.

particles entering the pores accumulated inside. The migration path of the particles at the pore throat inside the core changed, resulting in an obvious concentration tailing at the output end of the A5 core. In conclusion, selecting the injection parameters of the rock based on the pore-throat size of the FRET@SiO₂ nanoparticle tracer can effectively reduce its retention and improve the flow channel.

3.5.3. Effect of nanoparticle concentration on transport and retention

Different concentrations of fluorescent nano-tracer dispersions were injected into artificial cores to evaluate the effect of nanoparticle concentration on transport and retention. A fluorescent nano-tracer with a particle size of 50 nm was used in the experiment. Fig. 20 shows the breakthrough curves of the fluorescent silica nanoparticles at different concentrations. With the increase of injection concentration, the maximum relative concentration of fluorescent silica nanoparticles increased, corresponding penetration capacity increased, and retention rate in the core decreased. When the injection concentration is 10, 20 and 30 mg/L, retention rates for the three cores being 4.23%, 3.96%, and 3.72%, the maximum relative concentrations for the three cores were 0.96 (2.4 PV), 0.97 (2.43 PV), and 0.98 (2.45 PV), respectively. In Fig. 20(a)–(c) mark the results with significant differences. The differences in the retention rates of the FRET@SiO₂ nanoparticle tracer in the core at the three concentrations were greater than the significance level of 0.02; therefore, significant differences were observed in the FRET@SiO₂ nanoparticle tracer retention in the core at different injection concentrations. In all previous studies, reducing the zeta potential in porous media via nanofluid injection was considered the primary mechanism affecting nanofluid migration and retention. The above experimental results show that the charged properties of fluorescent silica nanoparticles and rock surface were negative and close to each other at the experimental pH (sandstone = −34.9 m/v, FRET@SiO₂ nanoparticle tracer = −37.3 m/v). During the injection process, this charge property did not affect the electronegativity of the rock surface. Reza (Hasannejada et al., 2017) proposed that this is because silica nanoparticles reduce the roughness of the pore walls of the rock during injection, thus reducing the complexity of its transport path through the rock. With an increase in the injection concentration, the contact area between the rock pore wall and the particles increases, resulting in a lower roughness of the rock pore wall; thus, more fluorescent silica nanoparticles are displaced, which is consistent with our experimental results. During the washing process of fluorescent silica nanoparticles, the relative concentration of the experimental core injected with a high concentration of fluorescent silica nanoparticles slowly decreased in the range of 3–4 PV, indicating that the high tracer concentration is more accessible to transport under this condition.

3.5.4. Effect of salinity on transport and retention

Several studies have shown that the presence of salt can significantly affect the transport behavior of nanoparticles because salinity influences the electrostatic repulsion between nanoparticles and rock surfaces (Hwang et al., 2012; Shiratori et al., 2009). Therefore, this study investigated the effect of salinity (1000 mg/L < TDS < 10000 mg/L) within the salinity range of water formation and injection on the transport of FRET@SiO₂ nanoparticle tracers. Fig. 21 shows the breakthrough curves and retention rates of the 10 mg/L FRET@SiO₂ nanoparticle tracer in the cores at different salinities. The penetration and retention rates of the FRET@SiO₂ nanoparticle tracer in the injection process increased with increasing salinity. As salinity increased from 1000 to 10000 mg/L, the maximum relative concentrations in the three

Table 3
Sensitive clay mineral content in the three natural cores (semi-quantitative calculation).

Core	Quartz, %	Albite, %	KAlSi ₃ O ₈ , %	Kaolinite, %	Montmorillonite, %	Clinochlore, %	Illite, %	Calcite, %
N1	25.67	62.34	7.88	4.11	0	0	0	0
N2	22.88	46.5	10.1	5.49	3.07	9.78	2.18	0
N3	54.99	13.01	0	5.29	7.17	16.28	3.26	0

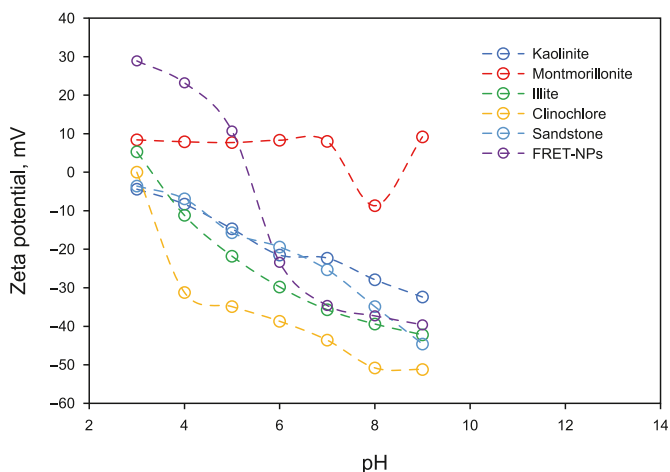


Fig. 16. Zeta potential changes in sandstone rocks, sensitive clay minerals, and FRET@SiO₂ nanoparticle tracers at different pH values.

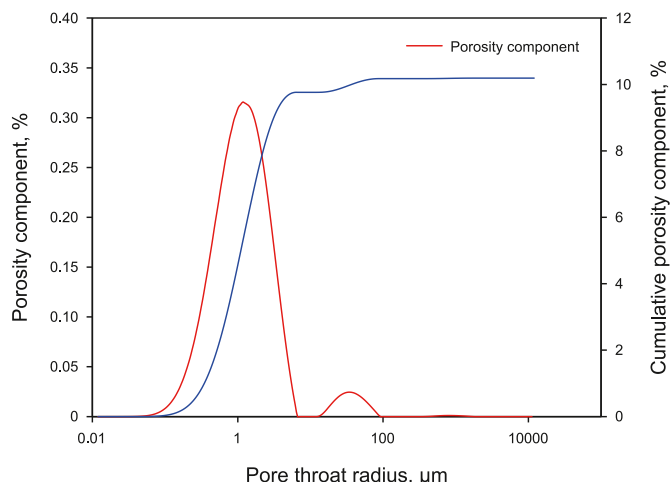


Fig. 18. Pore-throat and cumulative pore-throat distributions of experimental cores using core N1 as an example.

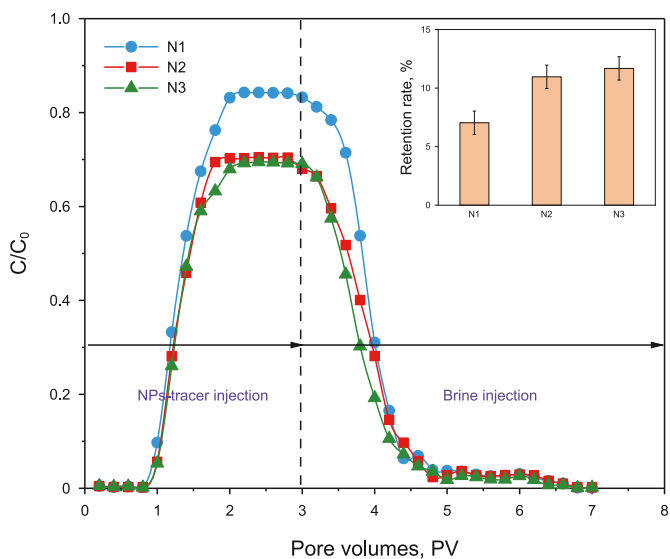


Fig. 17. Breakthrough curves of the FRET@SiO₂ nanoparticle tracer in natural sandstone cores.

cores were 0.86 (2.15 PV), 0.95 (2.38 PV), and 0.99 (2.48 PV), while the retention rates were 4.23%, 8.02%, and 14.26%, respectively. The zeta potential of the nanoparticles can explain the effect of salinity and is consistent with the DLVO theory (Becker et al., 2015). In the absence of electrolytes (i.e., in deionized water), the nanoparticles were stable and did not aggregate because of the strong electrostatic repulsion between the particles. Fig. 13 shows the zeta potential measurements with a decreased surface charge that increased with ionic strength, which reduced the energy barrier between the particles. Moreover, the influence of van der Waals gravity increased, resulting in particle aggregation. DLVO

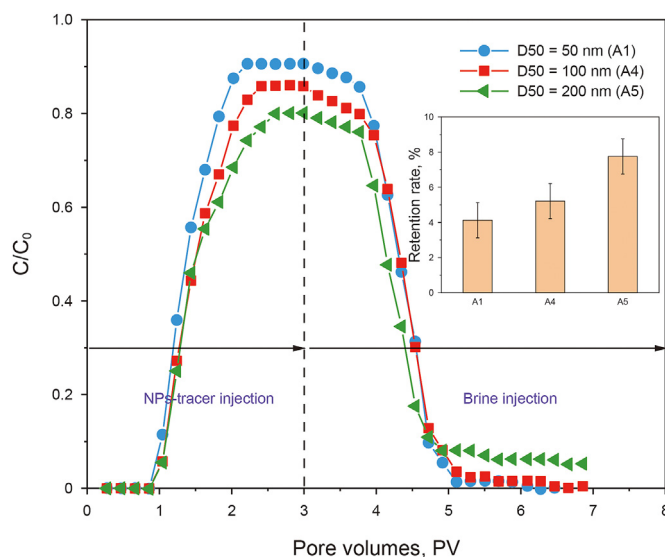


Fig. 19. Breakthrough curves and retention rates of different particle sizes.

calculations showed a secondary energy minimum, at which the depth increased with increasing ionic strength, thus favoring accumulation and resulting in the deposition of the resulting particle clusters (Ahmadi et al., 2011; Shen et al., 2014).

3.5.5. Effect of flow velocity on transport and retention

Fig. 22 shows the influence of the flow rate on the breakthrough curve and retention rate of the FRET@SiO₂ nanoparticle tracer. The chemical conditions of the background solution remained unchanged. When the flow rate increased from 0.2 to 1 mL/min, the maximum relative concentrations in the three cores were 0.86 (2.15 PV), 0.95 (2.38 PV), and 0.99 (2.48 PV), respectively.

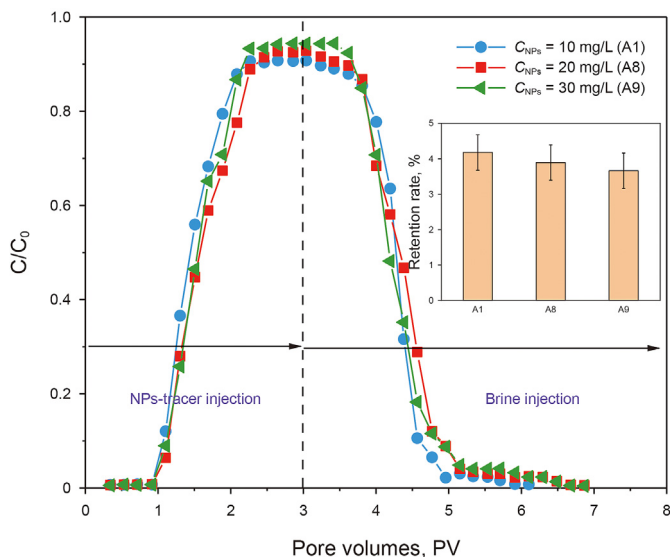


Fig. 20. Breakthrough curves and retention rates of the FRET@SiO₂ nanoparticle tracer with different concentrations.

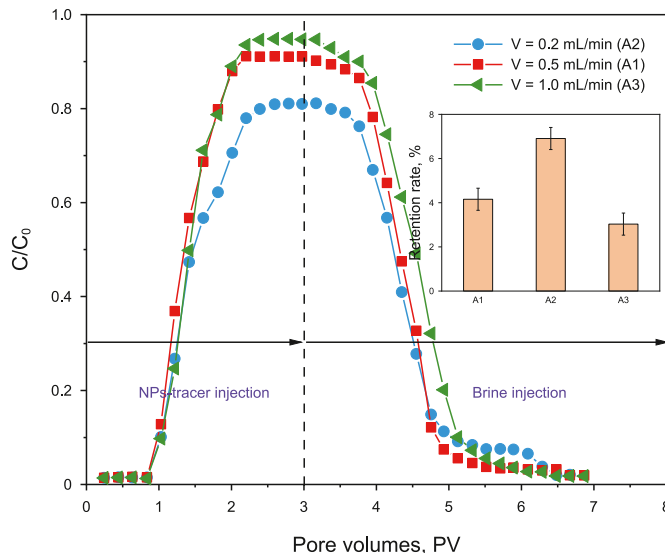


Fig. 22. Breakthrough curves and retention rates of the FRET@SiO₂ nanoparticle tracer at different flow rates.

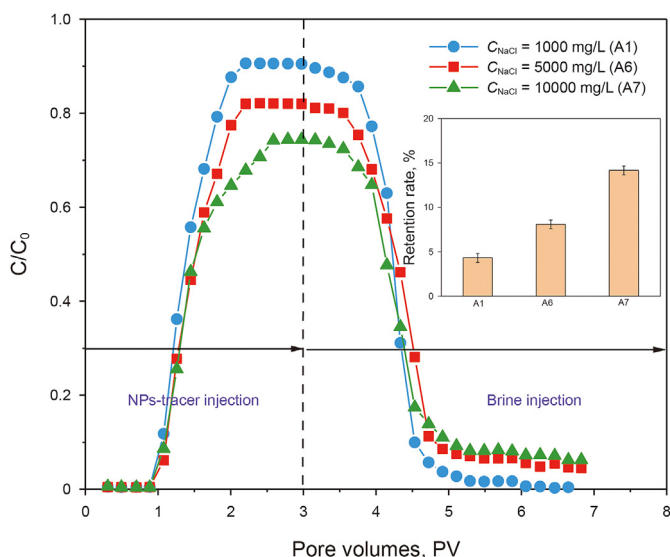


Fig. 21. Breakthrough curves and retention rates of FRET@SiO₂ nanoparticle tracers with different salinities.

Correspondingly, the retention rate in the medium decreased from 6.92% to 3.11%, indicating that with an increase in flow rate, the migration ability of fluorescent silica nanoparticles was enhanced and retention in the experimental core was reduced. The influence of the flow velocity on the transport of the FRET@SiO₂ nanoparticle tracer includes two aspects. First, an increase in flow rate reduces the residence time of particles in the medium, and the possibility of adsorption and retention on the surface of the medium is reduced. Second, an increase in flow velocity will enhance the shear force of the water flow, which will peel off some of the particles already attached to the surface of the medium, thus returning to the liquid phase.

When a fluorescent nano-tracer flows in the core, it is affected by hydrodynamic dispersion, which includes mechanical distribution and molecular diffusion. Molecular diffusion is not affected by velocity and occurs in the static state of the fluid. At low speeds,

hydrodynamic dispersion is primarily dominated by the molecular distribution. The movement of the tracer in the particle channel resulted in mechanical dispersion. From a microscopic perspective, the mechanical dispersion of the tracer is caused by the secondary polymerization of the tracer fluid after passing through a single pore. This process results in changes in the seepage velocity. When the flow rate was high, mechanical dispersion played a dominant role. The diffusion coefficient D is a function of the diffusion degree α and the flow velocity v of the flow medium. The diffusion coefficient of the fluorescent nano-tracer is calculated using formula $D = \alpha v$ to obtain $D = 0.31$. The diffusion degree α is negatively correlated with the flow rate. The higher the flow rate, the lower the diffusion degree of the tracer in sandstone, and the stronger the migration ability.

4. Conclusion

Chemical tracers that are used in oil fields cannot fully meet the needs of efficient injection and production monitoring of oil and gas reservoirs in terms of injection methods, types, and detection methods. Therefore, this study proposes a synthesis method for multicolor fluorescent silica nanoparticle tracers and evaluates their performance. The following conclusions were drawn from this study:

- (1) The synthesized multicolor fluorescent silica nano-tracer exhibits stable fluorescence characteristics under excitation at 450 nm, with the strongest emission peak at 576 nm.
- (2) The salinity of the dispersion was the primary factor affecting tracer dispersion. The higher the salinity, the poorer the dispersion and adaptability of the tracer to the reservoir salinity.
- (3) The fluorescence intensity of the tracer was primarily affected by the ambient temperature, and there was a negative linear correlation between the two.
- (4) Increases in tracer particle size and reservoir salinity, as well as decreases in injected tracer concentration and tracer inflow velocity resulted in an increase in tracer retention rate.

The multicolor fluorescent silica nanoparticle tracer synthesized

in this study has the advantages of high performance, versatility, low cost, and environmental friendliness. This tracer provides a new development idea for reservoir characterization and production monitoring and a promising solution for reservoir monitoring.

CRediT authorship contribution statement

Fang-Jun Jia: Writing – review & editing, Writing – original draft. **Hai-Tao Li:** Formal analysis, Conceptualization. **Zi-Min Liu:** Software, Methodology. **Xin Ma:** Visualization. **Guo-Qiang Zhang:** Investigation. **Qi-Hui Zhang:** Investigation. **Jie Li:** Investigation.

Declaration of competing interest

The authors declare that they have no known competing financial interests or personal relationships that could have appeared to influence the work reported in this paper.

Acknowledgement and funding

This study was funded by the Sichuan Science and Technology Education Joint Fund, including the mechanism and characterization of CO₂ geological storage and utilization of carbonate reservoirs in the Sichuan Basin to improve the sealing capacity of mudstone caprocks (No.2024NSFSC1981). It is also supported by the China Petroleum Science and Technology Innovation Fund, including the experiment of acoustic response mechanism of horizontal well fracturing and the research of DAS big data intelligent inversion method (No.2022DQ02-0305). This study is also supported by the National Natural Science Foundation of China 'Study on the mechanism of SNPs improving the sealing ability of mudstone caprock in CO₂ geological storage (No.42272176)'.

References

- Ahmadi, M., Khodadadi, M., Kord, M., et al., 2011. Zeta potential investigation and mathematical modeling of nanoparticles deposited on the rock surface to reduce fine migration. In: SPE Middle East Oil and Gas Show and Conference, Manama, Bahrain. <https://doi.org/10.2118/144139-MS>.
- Alaskar, M., Kosynkin, D., 2017. Successful crosswell field test of fluorescent carbonic nanoparticles. *J. Petrol. Sci. Eng.* 159, 443–450. <https://doi.org/10.1016/j.petrol.2017.09.006>.
- Alfataiege, A., Nguyen, T., Zhang, Y., et al., 2019. 3D hydraulic-fracture simulation integrated with 4D time-lapse multicomponent seismic and microseismic interpretations, Wattenberg field, Colorado (Conference Paper). *SPE Prod. Oper.* 34 (1), 57–71. <https://doi.org/10.2118/190448-PA>.
- Alqahtani, H., Vukovic, M., Djafer, A., et al., 2018. Characterization of ADOTS carbonic nanoparticle tracers before and after reservoir injection. *Conference Paper*. Proceedings - SPE Annual Technical Conference and Exhibition.
- Al-Qasim, A., Kokal, S., Hartvig, S., 2020. Subsurface monitoring and surveillance using inter-well gas tracers. *Upstream Oil Gas Technol.* 3, 100006. <https://doi.org/10.1016/j.uogt.2020.100006>.
- Al-Shalabi, E.W., Ouwendijk, S.M., Jerauld, G.R., et al., 2017. Single-well chemical-tracer modeling of low-salinity-water injection in carbonates. *SPE Reservoir Eval. Eng.* 20 (1), 118–133. <https://doi.org/10.2118/179515-PA>.
- App, J., 2017. Permeability, skin, and inflow-profile estimation from production-logging-tool temperature traces. *SPE J.* 22 (4), 1123–1133. <https://doi.org/10.2118/181254-PA>.
- Becker, M.D., Bormann, J.M., Sontag, J.J., et al., 2015. In situ measurement and simulation of nano-magnetite mobility in porous media subject to transient salinity. *Nanoscale* 7 (3), 1047–1057. <https://doi.org/10.1039/C4NR07032B>.
- Boersma, Q., Vachon, E., Boulesteix, T., 2020. Natural fault and fracture network characterization for the southern Ekofisk field: a case study integrating seismic attribute analysis with image log interpretation. *J. Struct. Geol.* 141, 104197. <https://doi.org/10.1016/j.jsg.2020.104197>.
- Bucior, D.A., 2013. Chemical tracers measure production from stimulated wells. *E & P: A Hart Energy Publication* 86 (7), 68–69.
- Chang, Z., Zhang, L., Wang, F., et al., 2018. Preparation and properties of artificial cores for experimental studies in reservoir engineering. *Rock Mech. Rock Eng.* 51 (9), 2779–2787. <https://doi.org/10.1007/s00603-018-1509-6>.
- Chen, L., Zhang, Z., Li, Y., et al., 2023. Fluorescent nanoparticle tracers for high-temperature and high-salinity reservoir characterization. *J. Petrol. Sci. Eng.* 217, 110723. <https://doi.org/10.1016/j.petrol.2022.110723>.
- Clemente, A., Fabbri, D., Lotti, M., et al., 2016. Fluorescently labeled SiO₂ nanoparticles as tracers in natural waters: dependence of detection limits on environmental conditions. *Environ. Sci.: Nano* 3 (3), 631–637. <https://doi.org/10.1039/C6EN00048A>.
- Davarpanah, A., Kharrat, R., Sadeghi, M., et al., 2018. Integrated production logging tools approach for convenient experimental individual layer permeability measurements in a multi-layered fractured reservoir. *J. Pet. Explor. Prod. Technol.* 8 (3), 743–751. <https://doi.org/10.1007/s13202-018-0472-2>.
- Dhir, A., Datta, A., 2016. FRET on surface of silica nanoparticle: effect of chromophore concentration on dynamics and efficiency. *J. Phys. Chem. C* 120 (36), 20125–20131. <https://doi.org/10.1021/acs.jpcc.6b06121>.
- Doorwar, S., Tagavifar, M., Dwarakanath, V., 2020. A 1D analytical solution to determine residual oil saturations from single-well chemical tracer test. *SPE Improved Oil Recovery Conference*. Chevron ETC.
- Frooqnia, A., 2011. Numerical Simulation and Interpretation of Production Logging Measurements Using A New Coupled Wellbore-Reservoir Model. In: *SPWLA 52nd Annual Logging Symposium*. Colorado Springs, Colorado.
- Haider, G., Zhang, J., Shirazi, S.A., 2021. The effects of particle size on solid particle erosion of elbows in low liquid and annular multiphase flow. *Corrosion* 66 (7), 065001.
- Hasanajjada, R., Pourafshary, P., Vatani, A., 2017. Application of silica nanofluid to control initiation of fines migration. *Petrol. Explor. Dev.* 44 (5), 850–859. <https://doi.org/10.1016/j.petrol.2017.05.009>.
- He, L., Zhang, L., Li, Q., et al., 2021. Investigation of fluorescence intensity and migration behavior of multi-functional nanoparticles in porous media. *J. Nanoparticle Res.* 23 (10), 257. <https://doi.org/10.1007/s11041-021-00475-9>.
- Hu, Z., Zhou, Y., Wang, J., et al., 2019. Carbon quantum dots with tracer-like breakthrough ability for reservoir characterization. *Sci. Total Environ.* 669, 579–589. <https://doi.org/10.1016/j.scitotenv.2019.03.181>.
- Hwang, C.C., Liu, Y., Zhang, L., et al., 2012. Highly stable carbon nanoparticles designed for downhole hydrocarbon detection. *Energy Environ. Sci.* 5 (8), 8304–8309. <https://doi.org/10.1039/C2EE02598K>.
- Jiang, X., Li, C., Zhang, L., et al., 2020. The effects of temperature and salinity on the aggregation and fluorescence properties of nanoparticles in complex fluid environments. *Nanotechnology* 30 (28), 285703. <https://doi.org/10.1088/1361-6528/ab9f0f>.
- Jongkittinarukorn, K., Kitcharoen, T., 2010. When Should We Run Production Logging Tool? *Chevron Corp.*
- Khaledialidusti, R., Kleppe, J., 2017. A comprehensive framework for the theoretical assessment of the single-well-chemical-tracer tests. *J. Petrol. Sci. Eng.* 159, 164–181. <https://doi.org/10.1016/j.petrol.2017.05.016>.
- Khan, S.A., Wang, Z., Wang, S., et al., 2022. Hydrophobic, partially hydrophobic, and hydrophilic ZnO/SiO₂ nanoparticles as fluorescent partitioning tracers for oil sensing applications. *J. Mol. Liq.* 360, 119505. <https://doi.org/10.1016/j.molliq.2022.119505>.
- Khurana, M., Yadav, A., Kumar, P., et al., 2020. Fluorescent resonance energy transfer-based sensors for environmental monitoring. *Sensors* 20 (9), 2557. <https://doi.org/10.3390/s20092557>.
- Ko, S., Huh, C., 2019. Use of nanoparticles for oil production applications. *J. Petrol. Sci. Eng.* 172, 97–114. <https://doi.org/10.1016/j.petrol.2018.11.010>.
- Kosynkin, D., Alaskar, M., 2016. Oil Industry First Interwell Trial of Reservoir Nanoagent Tracers. In: *SPE Annual Technical Conference and Exhibition, Saudi Aramco*.
- Lee, H., Choi, S., Lim, C., et al., 2022. Comparative study of fluorescence and absorbance-based methods for quantitative analysis of environmental pollutants. *Environ. Sci. Technol.* 56 (8), 5124–5133. <https://doi.org/10.1021/acs.est.1c05904>.
- Li, H., Liu, Z., Li, Y., et al., 2021. Evaluation of the release mechanism of sustained-release tracers and its application in horizontal well inflow profile monitoring. *ACS Omega* 6 (29), 19269–19280. <https://doi.org/10.1021/acsomega.1c02063>.
- Li, J., Zhang, Y., Wang, Z., et al., 2023. Improved sol-gel method for the synthesis of highly fluorescent silica nanoparticles for tracking in complex fluids. *J. Nanosci. Nanotechnol.* 23 (7), 1023–1031. <https://doi.org/10.1166/jnn.2023.19838>.
- Liu, Y., Wang, Z., Zhang, L., et al., 2018. Fluorescence-based nanoparticle tracers for monitoring reservoir characteristics. *J. Petrol. Sci. Eng.* 164, 345–357. <https://doi.org/10.1016/j.petrol.2017.06.017>.
- Li, Y., Wang, F., Zhang, Y., et al., 2021. Using cyclic alternating water injection to enhance oil recovery for carbonate reservoirs developed by linear horizontal well pattern. *Petrol. Explor. Dev.* 48 (5), 1139–1151. <https://doi.org/10.1016/j.petrol.2021.07.017>.
- Luo, H., Zhang, T., Liu, W., et al., 2020. A novel inversion approach for fracture parameters and inflow rates diagnosis in multistage fractured horizontal wells. *J. Pet. Sci. Eng.* 184, 106585. <https://doi.org/10.1016/j.petrol.2019.106585>.
- Luo, H., Zhang, T., Liu, W., et al., 2021. Simulated annealing algorithm-based inversion model to interpret flow rate profiles and fracture parameters for horizontal wells in unconventional gas reservoirs. *SPE J.* 26 (4), 1679–1699. <https://doi.org/10.2118/2021-1598-JPT>.
- Lu, Y., Zhang, J., Li, M., et al., 2022. Impact of fluid composition on the fluorescence intensity and transport of silica-based nanoparticles in reservoir conditions. *Colloids Surf. A Physicochem. Eng. Asp.* 634, 127902. <https://doi.org/10.1016/j.colsurfa.2022.127902>.
- Mari, J.L.O., Morel, P., Garcia, J., et al., 2021. Characterizing flow in the first hundred-meter depth of a fractured aquifer using hybrid seismic methods, acoustic logging, and flow-log measurements. *Oil Gas Sci. Technol.* 76, 18. <https://doi.org/10.2516/ogst/2021048>.

- Murugesan, S., Thomas, K., Gupta, A., et al., 2020. Unconventional Nanotechnology-Based Tracers for Drilling and Completion Applications. *International Petroleum Technology Conference, Baker Hughes*.
- Pareek, S., Sharma, P., Gupta, A., et al., 2020. Graphitic carbon nitride quantum dots (g-C₃N₄) to improve photovoltaic performance of polymer solar cell by combining Förster resonance energy transfer (FRET) and morphological effects. *Nano Express* 1 (1), 010057. <https://doi.org/10.1088/2632-233X/ab6f53>.
- Pazini, A., Gomes, L., Silva, C., et al., 2023. Synthesis of core-shell fluorescent silica nanoparticles with opposite surface charges for transport studies of nanofluids in porous media. *Colloids Surf. A Physicochem. Eng. Asp.* 670, 131586. <https://doi.org/10.1016/j.colsurfa.2023.131586>.
- Pedersen, T., Jensen, A., Rasmussen, J., 2021. A Single Well Chemical Tracer model that accounts for temperature gradients, pH changes and buffering. *J. Petrol. Sci. Eng.* 201, 108500. <https://doi.org/10.1016/j.petrol.2020.108500>.
- Sanni, M., Li, Q., Sun, J., et al., 2018. Pushing the envelope of residual oil measurement: a field case study of a new class of inter-well chemical tracers. *J. Petrol. Sci. Eng.* 163, 538–545. <https://doi.org/10.1016/j.petrol.2017.12.014>.
- Serres-Piole, C., Péliissier, F., Duc, M., et al., 2012. Water tracers in oilfield applications: guidelines. *J. Petrol. Sci. Eng.* 98–99, 22–39. <https://doi.org/10.1016/j.petrol.2012.08.009>.
- Sharma, A., Shook, G.M., Pope, G.A., 2014. *Rapid Analysis of Tracers for Use in EOR Flood Optimization*. Rex Energy Corporation, Chevron ETC, University of Texas At Austin.
- Shen, C., Wang, X., Zhang, J., et al., 2014. Heteroaggregation of microparticles with nanoparticles changes the chemical reversibility of the microparticles' attachment to planar surfaces. *J. Colloid Interface Sci.* 421, 103–113. <https://doi.org/10.1016/j.jcis.2014.01.014>.
- Shiratori, K., Yamashita, Y., Adachi, Y., 2009. Deposition and subsequent release of Na-kaolinite particles by adjusting pH in the column packed with Toyoura sand. *Colloids Surf. A* 306 (1–3), 137–141. <https://doi.org/10.1016/j.colsurfa.2007.09.067>.
- Silva, M., Stray, H., Bjørnstad, T., et al., 2018. Stability assessment of PITT tracer candidate compounds: the case of benzyl alcohols. *J. Petrol. Sci. Eng.* 167, 517–523. <https://doi.org/10.1016/j.petrol.2018.05.029>.
- Silva, M., Stray, H., Bjørnstad, T., et al., 2019. Stability assessment of PITT tracer candidate compounds – the case of pyrazines. *J. Pet. Sci. Eng.* 182, 106269. <https://doi.org/10.1016/j.petrol.2019.106269>.
- Stanzel, M., Schwarz, R., Steger, C., et al., 2019. Systematic study on FRET-pair functionalization of mesoporous thin films for correlation of pH-sensing and ionic mesopore accessibility. *Microporous Mesoporous Mater.* 282, 29–37. <https://doi.org/10.1016/j.micromeso.2019.03.022>.
- Sun, Y., Li, L., Zhang, J., et al., 2019. Synthesis of fluorescent silica nanoparticles for enhanced imaging and reservoir characterization. *J. Colloid Interface Sci.* 547, 91–100. <https://doi.org/10.1016/j.jcis.2019.04.075>.
- Tan, Y., Li, X., Wang, J., et al., 2019. Inflow characteristics of horizontal wells in sulfur gas reservoirs: a comprehensive experimental investigation. *Fuel* 238, 267–274. <https://doi.org/10.1016/j.fuel.2018.10.080>.
- Tayyib, D., Alshamrani, A., Al-Qunaibet, A., et al., 2019. *Overview of tracer applications in oil and gas industry. SPE Kuwait Oil & Gas Show and Conference*.
- Velasco-Lozano, M., Balhoff, M.T., 2023. Modeling of chemical tracers for two-phase flow in capillary-dominated porous media. *Fuel* 339, 127421. <https://doi.org/10.1016/j.fuel.2023.127421>.
- Vitorge, E., Anzalone, A., Delubac, A., et al., 2013. Size- and concentration-dependent deposition of fluorescent silica colloids in saturated sand columns: transport experiments and modeling. *Environ. Sci. Process. Impacts.* 15 (8), 1590–1600. <https://doi.org/10.1039/c3em00311g>.
- Vitorge, E., Anzalone, A., Delubac, A., et al., 2014. Comparison of three labeled silica nanoparticles used as tracers in transport experiments in porous media. Part I: syntheses and characterizations. *Environ. Pollut.* 184, 605–612. <https://doi.org/10.1016/j.envpol.2013.06.037>.
- Wang, C., 2021. Study on water injection effect of new reservoir for petroleum energy development. *IOP Conf. Ser. Earth Environ. Sci.* 770, 012040. <https://doi.org/10.1088/1755-1315/770/1/012040>.
- Wang, J., Zhou, Q., Li, Y., et al., 2023. Fluorescence vs absorbance detection: a comparison of detection limits and analytical performance in biomolecular assays. *Biosens. Bioelectron.* 215, 114451. <https://doi.org/10.1016/j.bios.2023.114451>.
- Wang, L., Liu, X., Zhang, H., et al., 2019. Experimental study of artificial porous media: core fabrication and characterization techniques. *J. Hydrol.* 568, 262–272. <https://doi.org/10.1016/j.jhydrol.2018.11.048>.
- Wang, L., Liu, Y., Zhang, Y., et al., 2021. Fluorescent silica nanoparticles synthesized by improved sol-gel method for environmental monitoring applications. *Environ. Monit. Assess.* 193 (8), 254. <https://doi.org/10.1007/s10661-021-08909-9>.
- Wang, X., Li, H., Zhang, J., et al., 2023. Factors controlling spatial distribution of complex lithology in transitional shale strata: implications from logging and 3D seismic data, Shan-2 Lower Sub-member, Eastern Ordos Basin. *Front. Earth Sci.* 10. <https://doi.org/10.3389/feart.2023.999500>.
- Xie, J., Zhang, L., Li, Y., et al., 2020. Effects of temperature and salinity on the dispersion and stability of silica nanoparticles in porous media. *J. Colloid Interface Sci.* 563, 299–307. <https://doi.org/10.1016/j.jcis.2020.01.036>.
- Xu, Y., Zhang, L., Li, W., et al., 2022. Synthesis and application of multifunctional fluorescent nanoparticles for environmental monitoring. *Environ. Sci. Technol.* 56 (11), 7024–7032. <https://doi.org/10.1021/acs.est.2c01634>.
- Yang, H., Liu, Y., Wang, Z., et al., 2020. Influence mechanism of fluorescent monomer on the performance of polymer microspheres. *J. Mol. Liq.* 308, 113081. <https://doi.org/10.1016/j.molliq.2020.113081>.
- Yang, L., Liu, Y., Wang, Y., et al., 2021. Fluorescence versus absorbance in nanoparticle-based assays: sensitivity, selectivity, and detection limits. *Sensor. Actuator. B Chem.* 349, 130748. <https://doi.org/10.1016/j.snb.2021.130748>.
- Yi, H., Zhang, L., Wang, S., et al., 2021. Using cyclic alternating water injection to enhance oil recovery for carbonate reservoirs developed by linear horizontal well pattern. *Petrol. Explor. Dev.* 48 (4), 1139–1151. [https://doi.org/10.1016/s1876-3804\(21\)60097-6](https://doi.org/10.1016/s1876-3804(21)60097-6).
- Zhang, R., Wei, S., Shao, L., et al., 2022. Imaging intracellular drug/siRNA co-delivery by self-assembly cross-linked polyethylenimine with fluorescent core-shell silica nanoparticles. *Polymers* 14 (9), 1813. <https://doi.org/10.3390/polym14091813>.
- Zhang, Z., Zhang, X., Zheng, Q., et al., 2024. A non-residue surface modification strategy for active-targeting fluorescent silica nanoparticles to cellular organelles. *Microchim. Acta.* 191 (4), 181. <https://doi.org/10.1007/s00604-024-06239-x>.
- Zhao, H., Zhang, Y., Liu, H., et al., 2016. History matching and production optimization of water flooding based on a data-driven interwell numerical simulation model. *J. Nat. Gas Sci. Eng.* 31, 48–66. <https://doi.org/10.1016/j.jngse.2016.02.043>.